Article

Molecular Cell

Autism-Misregulated eIF4G Microexons Control Synaptic Translation and Higher Order Cognitive Functions

Graphical Abstract

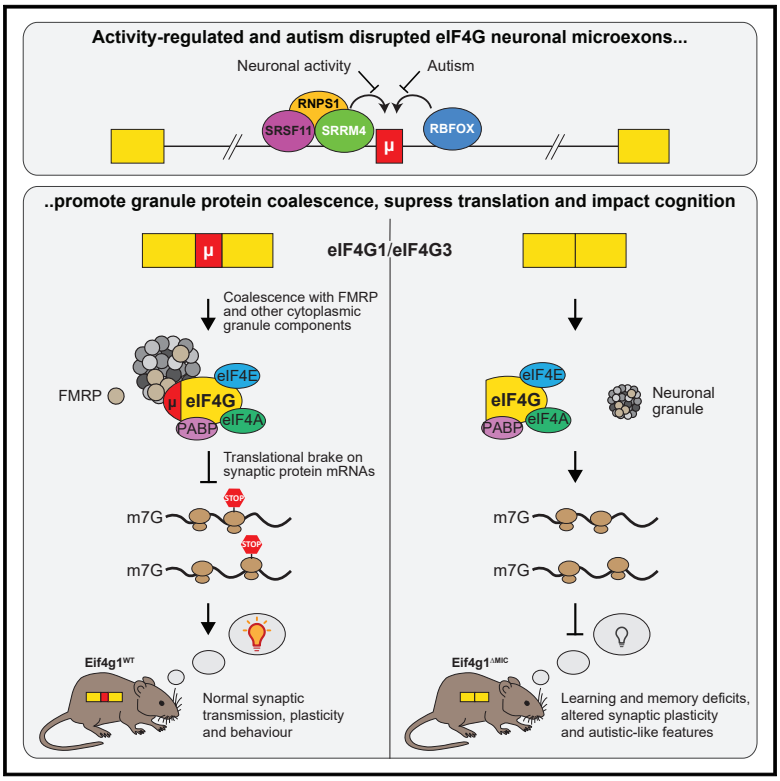

Highlights

- Autism-disrupted eIF4G microexons mediate activity-dependent responses
- eIF4G microexons suppress the expression of critical synaptic proteins
- eIF4G microexon-deficient mice display social behavior and memory deficits
- eIF4G microexons coalesce with neuronal granule components and stall ribosomes

Authors

Thomas Gonatopoulos-Pournatzis, Rieko Niibori, Eric W. Salter, ..., Melanie A. Woodin, Sabine P. Cordes, Benjamin J. Blencowe

Correspondence

t.gonatopoulos@gmail.com (T.G.-P.), cordes@lunenfeld.ca (S.P.C.), b.blencowe@utoronto.ca (B.J.B.)

In Brief

Gonatopoulos-Pournatzis et al. demonstrate that conserved, autism-disrupted microexons in eIF4G translation initiation factors regulate the neuronal proteome and control higher order cognitive functions. The microexons function as a translational brake and elicit ribosome stalling on transcripts encoding synaptic proteins through their propensity to coalesce with FMRP and other neuronal granule components.

Gonatopoulos-Pournatzis et al., 2020, Molecular Cell 77, 1176–1192
March 19, 2020
https://doi.org/10.1016/j.molcel.2020.01.006

CellPress

CellPress

Molecular Cell
Article

Autism-Misregulated eIF4G Microexons Control Synaptic Translation and Higher Order Cognitive Functions

Thomas Gonatopoulos-Pournatzis,[1,*] Rieko Niibori,[2,16] Eric W. Salter,[2,3,16] Robert J. Weatheritt,[1,4,5,16] Brian Tsang,[6,7,16] Shaghayegh Farhangmehr,[1,8,16] Xinyi Liang,[9] Ulrich Braunschweig,[1] Jonathan Roth,[1,2,8] Shen Zhang,[2] Tyler Henderson,[2,8] Eesha Sharma,[1,8] Mathieu Quesnel-Vallières,[1,8] Jon Permanyer,[10] Stefan Maier,[2] John Georgiou,[2] Manuel Irimia,[10,11,12] Nahum Sonenberg,[13,14] Julie D. Forman-Kay,[6,7] Anne-Claude Gingras,[2,8] Graham L. Collingridge,[2,3,15] Melanie A. Woodin,[9] Sabine P. Cordes,[2,8,*] and Benjamin J. Blencowe[1,8,17,*]

[1]Donnelly Centre, University of Toronto, Toronto, ON M5S 3E1, Canada
[2]Lunenfeld-Tanenbaum Research Institute, Mount Sinai Hospital, Toronto, ON M5G 1X5, Canada
[3]Department of Physiology, University of Toronto, Toronto, ON M5S 1A8, Canada
[4]EMBL Australia, Garvan Institute of Medical Research, Darlinghurst, NSW 2010, Australia
[5]St. Vincent's Clinical School, University of New South Wales, Sydney, NSW 2010, Australia
[6]Program in Molecular Medicine, The Hospital for Sick Children, Toronto, ON M5G 0A4, Canada
[7]Department of Biochemistry, University of Toronto, Toronto, ON M5S 1A8, Canada
[8]Department of Molecular Genetics, University of Toronto, Toronto, ON M5S 1A8, Canada
[9]Department of Cell and Systems Biology, University of Toronto, Toronto, ON M5S 3G5, Canada
[10]Centre for Genomic Regulation, Barcelona 08003, Spain
[11]Universitat Pompeu Fabra (UPF), Barcelona 08002, Spain
[12]ICREA, Barcelona 08010, Spain
[13]Goodman Cancer Research Center, McGill University, Montreal, QC H3A 1A3, Canada
[14]Department of Biochemistry, McGill University, Montreal, QC H3G 1Y6, Canada
[15]Tanz Centre for Research in Neurodegenerative Diseases, University of Toronto, Toronto, ON M5S 1A8, Canada
[16]These authors contributed equally
[17]Lead Contact
*Correspondence: t.gonatopoulos@gmail.com (T.G.-P.), cordes@lunenfeld.ca (S.P.C.), b.blencowe@utoronto.ca (B.J.B.)
https://doi.org/10.1016/j.molcel.2020.01.006

SUMMARY

Microexons represent the most highly conserved class of alternative splicing, yet their functions are poorly understood. Here, we focus on closely related neuronal microexons overlapping prion-like domains in the translation initiation factors, eIF4G1 and eIF4G3, the splicing of which is activity dependent and frequently disrupted in autism. CRISPR-Cas9 deletion of these microexons selectively upregulates synaptic proteins that control neuronal activity and plasticity and further triggers a gene expression program mirroring that of activated neurons. Mice lacking the Eif4g1 microexon display social behavior, learning, and memory deficits, accompanied by altered hippocampal synaptic plasticity. We provide evidence that the eIF4G microexons function as a translational brake by causing ribosome stalling, through their propensity to promote the coalescence of cytoplasmic granule components associated with translation repression, including the fragile X mental retardation protein FMRP. The results thus reveal an autism-disrupted mechanism by which alternative splicing specializes neuronal translation to control higher order cognitive functioning.

INTRODUCTION

Alternative splicing has critical roles in numerous fundamental biological processes (Baralle and Giudice, 2017; Scotti and Swanson, 2016; Ule and Blencowe, 2019; Vuong et al., 2016). This is especially the case in the mammalian brain, which expresses among the most complex and conserved alternative splicing programs (Barbosa-Morais et al., 2012; Merkin et al., 2012), the disruption of which plays a causative or contributing role to different neurological diseases and disorders (Licatalosi and Darnell, 2010; Nussbacher et al., 2015; Quesnel-Vallières et al., 2019; Sibley et al., 2016; Vuong et al., 2016). However, only a small number of neural-regulated alternative splicing events have been functionally characterized (Raj and Blencowe, 2015; Ustianenko et al., 2017; Vuong et al., 2016).

We previously detected a program of 3–27 nucleotide neuronal microexons that is primarily controlled by the serine/arginine repetitive matrix protein 4 (SRRM4) (also known as nSR100; Calarco et al., 2009; Gonatopoulos-Pournatzis et al., 2018; Irimia et al., 2014; Quesnel-Vallières et al., 2015, 2016). Neuronal microexons are highly conserved at the levels of both sequence and regulatory characteristics. The majority are located within and preserve open reading frames, and they invariably are located on protein surfaces, where they participate in the regulation of protein-protein interactions (Dergai et al., 2010; Irimia et al., 2014; Li et al., 2015; Ohnishi et al., 2014; Toffolo et al., 2014). Approximately one-third of neuronal

microexons show increased skipping, concordant with decreased levels of expression of SRRM4, in the brains of individuals that primarily have idiopathic forms of autism spectrum disorder (ASD) (Irimia et al., 2014). Mice haploinsufficient for SRRM4 recapitulate microexon misregulation and display multiple ASD-like phenotypes, including altered social behavior, increased sensitivity to environmental stimuli, and altered synaptic spine density and transmission (Quesnel-Vallières et al., 2015, 2016). These observations, and the finding that microexons are enriched in genes with genetic links to ASD (Irimia et al., 2014), have prompted important questions, including: what are their individual roles, which contribute to ASD-associated phenotypes, and what are the mechanisms by which they function?

In addition to altered splicing, misregulation of translation is a recurring mechanism associated with ASD (Bagni and Zukin, 2019; Borrie et al., 2017; Holt and Schuman, 2013; Jung et al., 2014; Richter et al., 2015; Santini and Klann, 2014). In fragile X syndrome (FXS), the most common form of syndromic autism, repeat expansions in the *FMR1* gene reduce the translation-repressive activity of its product, FMRP. This results in altered synaptic protein synthesis, plasticity, and ASD-associated phenotypes (Bakker et al., 1994; Darnell et al., 2011; Feng et al., 1995; Huber et al., 2002). Tuberous sclerosis, a genetic disorder caused by loss-of-function mutations in *TSC1* or *TSC2* genes, is frequently characterized by autistic-like phenotypes that can be rescued by pharmacomodulation of mTOR signaling, which controls translation initiation (Auerbach et al., 2011; Borrie et al., 2017; Ehninger et al., 2008). The role of altered translational control in ASD is further supported by the discovery of mutations in *PTEN* and the cap binding initiation factor *eIF4E* (Neves-Pereira et al., 2009; Zhou and Parada, 2012), and from the observation of ASD-like phenotypes in mouse models with genetic alterations that result in increased cap-dependent translation in neurons (Gkogkas et al., 2013; Santini et al., 2013). An important question is whether ASD-associated altered splicing patterns, including those involving microexons, might also impact neuronal translation to result in autistic phenotypes. In this regard, a more general question is whether regulated alternative splicing contributes to the control of the translational outputs that underlie neurodevelopmental and behavioral phenotypes.

We have addressed these questions through investigation of previously uncharacterized, ASD-misregulated microexons in the eukaryotic translation initiation factors 4 gamma, eIF4G1 and eIF4G3, paralogs. eIF4G proteins interact with eIF4E and the eIF4A DEAD-box RNA helicase to form a heterotrimeric eIF4F complex required for translation initiation (Gingras et al., 1999). Deletion of the eIF4G microexons specifically upregulates the translation of numerous proteins that control synaptic transmission and neuronal activity, including the obligatory NMDA receptor subunit GluN1, which controls calcium influx in neurons, synaptic plasticity, and memory formation. These changes contribute to an activated neuronal state and strengthen synaptic connectivity. Consistently, mice deficient of the eIF4G1 microexon show altered social behavior, memory, and learning deficits. Inclusion of the microexons promotes ribosome stalling on translationally repressed synaptic protein transcripts that significantly overlap binding targets of FMRP, whereas their skipping, which is activity-dependent and observed in the brains of ASD subjects, relieves this repression. Consistent with these observations, the eIF4G1 microexon promotes the coalescence of components of neuronal granules associated with translation repression, including FMRP. Collectively, the results demonstrate a critical function for individual alternative microexons in the specialization of neuronal translation and animal behavior. They further suggest that disruption of protein synthesis outputs, controlled by microexon-dependent changes in multivalent interactions with neuronal granule components, may commonly arise in ASD.

RESULTS

A Neuronal Microexon Switch in eIF4G Translation Initiation Factors

To investigate possible roles for alternative splicing in the functional specialization of translation, we performed an analysis of RNA sequencing (RNA-seq) data from ~30 diverse cell and tissue types in human and mouse for regulated splicing events that potentially affect ribosome assembly and core ribosomal proteins. This reveals 227 alternative splicing events, 32 of which are conserved in mammals (Table S1) and several of which display pronounced neuronal-specific differential regulation (Figure 1A). Among the latter events are previously reported microexons in the small ribosomal subunit protein 24 (RPS24) and cytoplasmic polyadenylation element binding protein 4 (CPEB4) (Figures S1A and S1B; Gupta and Warner, 2014; Parras et al., 2018). However, two of the events correspond to previously uncharacterized microexons. These are each predicted to insert seven amino acids with the closely related sequences, GGFRSLQ and GGFRPIQ, proximal to the N-termini of eIF4G1 and eIF4G3, respectively (Figure 1B).

The eIF4G microexons individually display conservation at the levels of amino acid sequence and neuronal-differential splicing across vertebrates spanning at least 450 Ma of evolution (Figures 1C and S1B–S1F). In contrast, a third eIF4G paralog, eIF4G2/DAP5/p97, lacks the N-terminal microexon-containing region found in eIF4G1 and eIF4G3. eIF4G1 and eIF4G3 act as scaffolds in the formation of productive initiation complexes (see Introduction; Gingras et al., 1999). Given their high degree of conservation, we hypothesized that differential regulation of the eIF4G1 and eIF4G3 microexons may be important for controlling neuronal-specific translation and consequently brain function.

A Regulatory Network Genetically Associated with Neurological Disorders Controls eIF4G Microexon Splicing

To explore possible roles of the eIF4G microexons, we initially investigated their regulation. Neuronal microexons are frequently controlled by a complex consisting of SRRM4, SRSF11, and RNPS1, whereas RBFOX regulates an overlapping although distinct and smaller subset of microexons (Gonatopoulos-Pournatzis et al., 2018; Li et al., 2015). Consistent with these findings, the expression level of Srrm4 closely tracks increased levels of splicing of both exons during glutamatergic neuronal differentiation (Figures 1C, S1A, and S1B). Moreover, both exons show decreased splicing in the brains of *Srrm4*-knockout mice

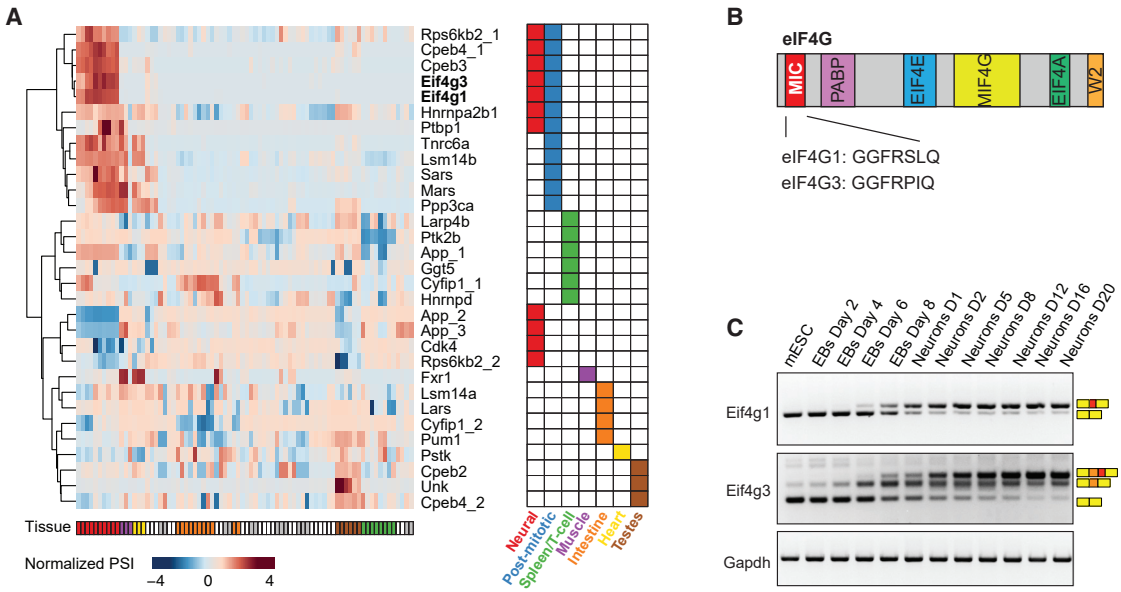

Figure 1. Identification of Neuronal-Specific Microexons in eIF4G Paralogs

(A) Heatmap showing percent spliced in (PSI) of alternative splicing events in transcripts encoding translation-related factor genes across ~30 diverse mouse cell and tissue types (see Table S1); tissue specificity of increased PSI is indicated in the right panel.

(B) Schematic of eIF4G functional regions and microexon (MIC) location. The amino acid sequence encoded by the microexons is indicated.

(C) RT-PCR assays monitoring Eif4g1 and Eif4g3 microexon splicing during neuronal differentiation of CGR8 mouse embryonic stem cells (mESCs). Amplified spliced products are shown adjacent to each gel. Red rectangle, microexon; orange rectangle, adjacent alternative exon. Expression of Gapdh is shown as a loading and recovery control.

(Figure S2A), and ectopic expression of Srrm4 is sufficient to activate microexon splicing in mouse embryonic stem cells (mESCs) (Figure 2A). Furthermore, knockdown of endogenous Srrm4, Srrm3 (a paralog of Srrm4), Rnps1, Srsf11, and Rbfox2 all result in skipping of the Eif4g microexons in N2A cells, whereas knockdown of Ptbp1, a widely acting repressor of neuronal alternative splicing (Vuong et al., 2016), increases the inclusion levels of these exons (Figures 2B, S2B, and S2C).

To assess whether Srrm4, Srrm3, Rnps1, and Srsf11 directly activate Eif4g1 and Eif4g3 microexon splicing, we performed an individual nucleotide resolution crosslinking and immunoprecipitation coupled to sequencing (iCLIP-seq) analysis of these factors. Srrm4, Srrm3, and Srsf11, but not GFP (analyzed as a negative control), form binding peaks proximally upstream of both microexons, supporting a direct role in their regulation (Figures 2C, 2D, S2D, and S2E; Gonatopoulos-Pournatzis et al., 2018; Irimia et al., 2014; Raj et al., 2014). Moreover, consistent with its distinct binding map and mechanism of action (Lee et al., 2016; Lovci et al., 2013; Weyn-Vanhentenryck et al., 2014), Rbfox forms spatially distinct binding peaks downstream of the Eif4g1 and Eif4g3 microexons (Figures 2D and S2E).

Chromatin regulators, such as Ep300, control Srrm4 expression (Gonatopoulos-Pournatzis et al., 2018). Consistently, its ablation also affects Eif4g1 microexon splicing (Figure S2C). Notably, sequencing studies have identified mutations or risk alleles in *SRRM4*, *SRRM3*, *SRSF11*, *RNPS1*, *RBFOX1*, and *EP300* that are linked to neurological disorders, including autism and intellectual disability (C Yuen et al., 2017; Iossifov et al., 2014; Lim et al., 2017; Lucariello et al., 2016; Nguyen et al., 2013; De Rubeis et al., 2014; S.W. Scherer and R. Yuen, personal communication). Collectively, these results provide evidence that a network of chromatin and splicing factors impacted in ASD regulate the splicing of EIF4G microexons.

EIF4G Microexon Splicing Is Activity Dependent and Disrupted in Autistic Brains

SRRM4 levels decrease upon induced neuronal activity, leading to the proposal that diverse genetic alterations resulting in increased neuronal activity may frequently disrupt microexon splicing in autistic patients (Quesnel-Vallières et al., 2016). Moreover, RBFOX subcellular localization and thus its splicing function are also regulated by neuronal activity (Lee et al., 2009). Accordingly, we next asked whether neuronal activity impacts the splicing of the EIF4G microexons. Indeed, depolarization of neurons with KCl, or treatment with the ionotropic glutamate receptor agonists kainate and domoic acid, leads to a rapid and marked decrease in splicing of the Eif4g1 and Eif4g3 microexons in a transcription-dependent manner (Figures 2E, S2F, and S2G). These results thus suggest that the eIF4G microexons are dynamically regulated in response to neuronal activity.

Analysis of RNA-seq data reveals disrupted splicing of the EIF4G1 exon in a subset of autistic patients (Figure S2H; Irimia et al., 2014). Expanding this analysis to a larger cohort (58 ASD and matched control subjects) using PsychENCODE RNA-seq (Gandal et al., 2018) confirmed a significant reduction in splicing of the EIF4G1 microexon in ASD compared to control subjects ($p < 3.89 \times 10^{-4}$; Mann-Whitney U test; Figure 2F). In contrast, the splicing levels of the EIF4G3 microexon are not significantly

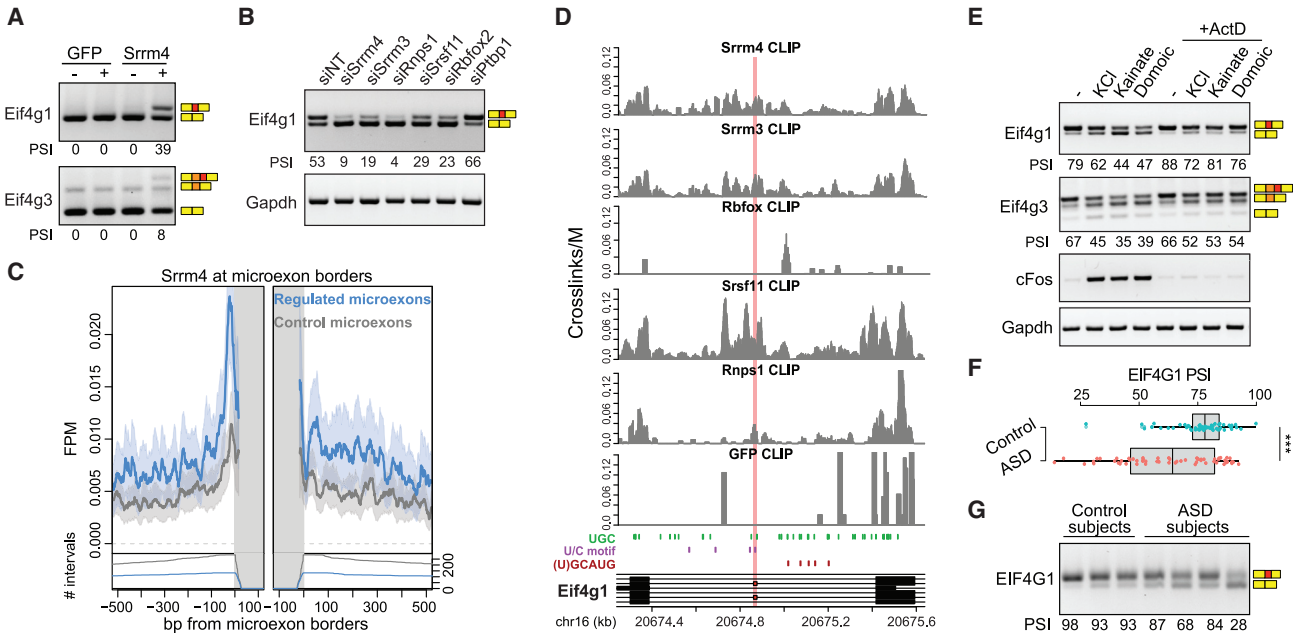

Figure 2. Srrm4 and Neuronal Activity Dynamically Regulate EIF4G Microexon Splicing

(A) RT-PCR assays monitoring Eif4g1 and Eif4g3 microexon splicing in CGR8 mESCs engineered to express GFP or Srrm4 in a doxycycline-inducible manner.

(B) RT-PCR assays monitoring Eif4g1 microexon splicing in N2A cells transfected with the indicated small interfering RNAs (siRNAs).

(C) Average signal for iCLIP reads recovered from Flag-Srrm4 protein expressed in mESC-derived neurons (day *in vitro* [DIV] 10). Mapped reads surrounding microexons regulated (blue line) or not regulated (gray line) by Srrm4 are shown.

(D) Mapped reads surrounding the Eif4g1 microexon from iCLIP experiments analyzing Srrm4, Srrm3, Srsf11, Rnps1, Rbfox, and GFP proteins (from neurons or N2A cells) are shown.

(E) RT-PCR assays monitoring Eif4g1 and Eif4g3 microexons in mESC-derived neurons (DIV 12) treated with KCl (55 mM), kainate (20 μM), or domoic acid (20 μM) for 6 h in the presence or absence of actinomycin D (5 μg/mL).

(F) PSI of EIF4G1 microexon in brain tissue from controls (n = 58) and individuals with ASD (n = 58); Mann-Whitney U test; $p < 0.000389$.

(G) RT-PCR assays monitoring EIF4G1 microexon using RNA samples from *post mortem* patient brain cortex (superior temporal gyrus; ba41/42/22) from ASD and control individuals.

different between ASD and control individuals (Figure S2I). Disruption of EIF4G1 microexon splicing was confirmed by RT-PCR analysis of a subset of available RNA samples from the RNA-seq profiled ASD and control subjects (Figure 2G). Notably, the EIF4G1 microexon ranks as the third most strongly disrupted of 35 microexons with detected significant reductions in splicing levels in the brains of ASD versus control subjects (Figure S2J). Collectively, these data suggest that disruption of EIF4G1 microexon splicing may contribute to molecular changes and phenotypes associated with autism.

eIF4G Microexons Regulate the Expression of Synaptic Proteins

To investigate whether the eIF4G microexons function to control neuronal translation, CRISPR-Cas9 editing was used to delete both exons in mESCs, which were subsequently differentiated into neurons. Because eIF4G1 and eIF4G3 possess similar biochemical activities (Gingras et al., 1999), double microexon-knockout (DKO) cell lines were generated to eliminate potential compensatory mechanisms. The DKO neurons were subjected to isobaric labeling and quantitative mass spectrometry (Figures 3A, 3B, and S3A–S3D). Relative to control neurons, ~350 proteins (representing ~10% of total detected proteins) display significant changes (false discovery rate [FDR] < 0.01) in steady-state levels in the DKO neurons, with more accentuated differences at a later time point of neuronal differentiation when functional synapses are formed (Figures 3C and S3E; Table S2). Notably, proteins with increased expression in the DKO neurons are significantly enriched in synaptic functions (Figures 3C and 3D; $p < 6.18 \times 10^{-06}$; Fisher's exact test). These include the obligatory subunit of the ionotropic glutamate NMDA receptor, GluN1 (encoded by *Grin1*), which is critical for major forms of synaptic plasticity and controls learning and memory (Tsien et al., 1996; Volianskis et al., 2015). Critical postsynaptic components of inhibitory synapses, including Gephyrin and Neuroligin-2 (Tyagarajan and Fritschy, 2014), also display increased protein levels in the DKO neurons (Figure S3F; Table S2). Increased expression of these proteins was confirmed by western blotting (Figures 3E and 3F). These results thus reveal that the eIF4G microexons control the expression of numerous synaptic proteins, including NMDA receptors that govern activity-dependent responses underlying learning and memory.

Consistent with deletion of the eIF4G1 and eIF4G3 microexons impacting the expression of the affected proteins at the translational level, RNA-seq profiling of the DKO neurons does not reveal appreciable changes in steady-state levels of the

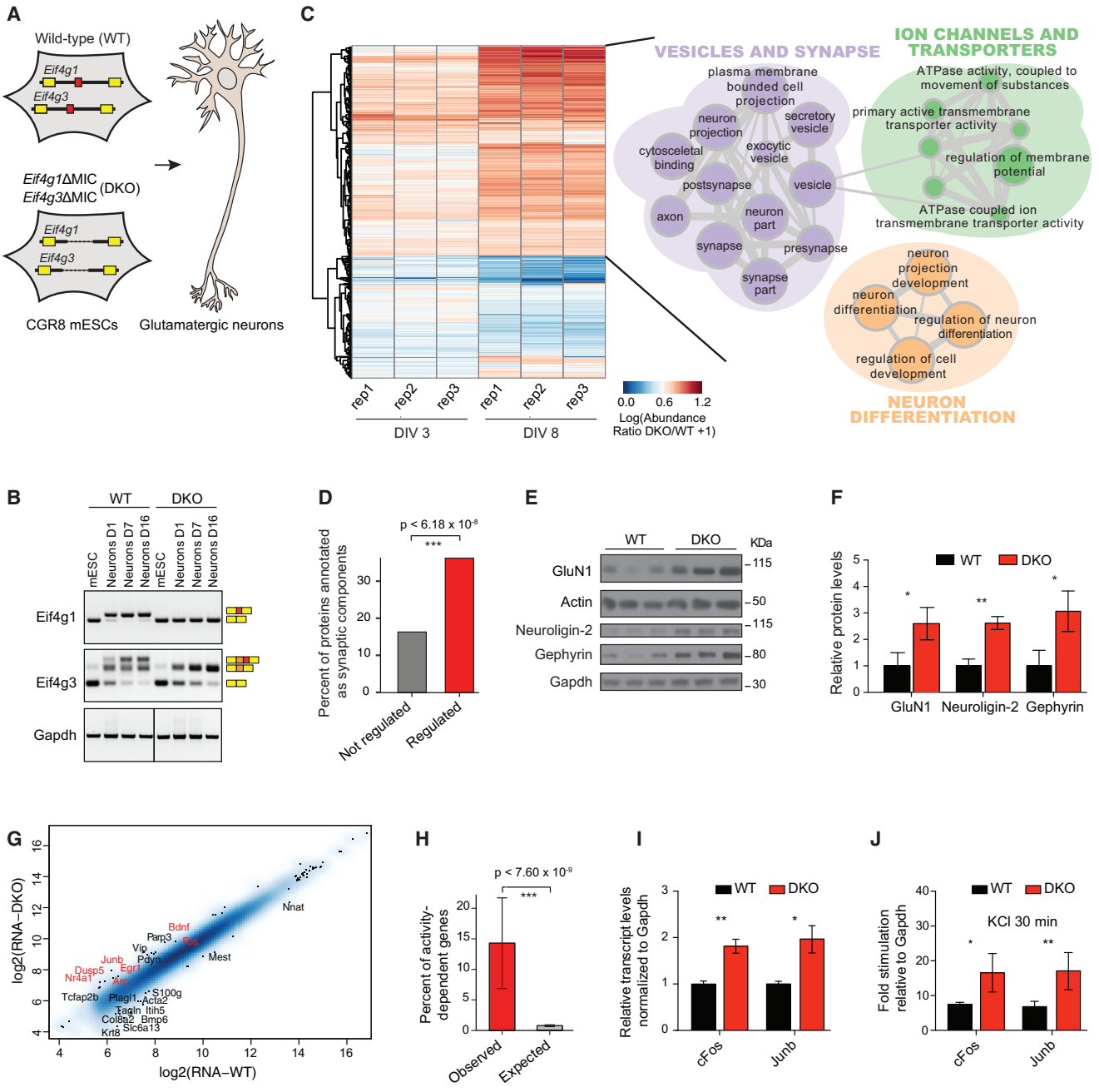

Figure 3. eIF4G Microexons Control the Expression of Synaptic Receptors Linked to the Regulation of Neuronal Activity

(A) Overview of experimental strategy for the generation of wild-type (WT) or double *Eif4g1* and *Eif4g3* microexon-deficient (DKO) mESC-derived neurons.

(B) RT-PCR assays monitoring Eif4g1 and Eif4g3 microexon splicing during neuronal differentiation of a WT and DKO CGR8 mESC clonal line.

(C) Proteins differentially expressed between WT and DKO neurons as determined by quantitative mass spectrometry (MS). Three biological replicates of each genotype were analyzed, and the abundance ratio of differentially expressed proteins is shown (left panel). Analysis of Gene Ontology term enrichment among proteins whose expression is repressed by eIF4G microexons (right panel) is shown.

(D) Percentage of eIF4G microexon-regulated proteins that overlap synaptic proteins (Pirooznia et al., 2012) compared to MS-detected proteins not regulated by eIF4G microexons ($p < 0.001$; Fisher's exact test).

(E and F) Western blots (E) and quantification of relative expression (F) of GluN1, Gephyrin, and Neuroligin-2 protein levels in WT and DKO neurons. Immunoblotting of Actin and Gapdh are shown to control for loading and recovery. Error bars, SD; *$p < 0.05$; **$p < 0.01$; two-tailed t test.

(G) Log2 mRNA abundance plotted for WT and DKO mESC-derived neurons. Genes with significant differential expression (FDR < 0.05) are indicated by black dots, and representative gene names are shown. Activity-dependent genes are indicated in red.

(legend continued on next page)

corresponding mRNAs (Figure 3G; Table S3). Notably, however, genes with transcript level changes significantly overlap those regulated by neuronal activity, as determined by comparison with gene expression changes detected after KCl depolarization of primary neurons (Figures 3G and 3H; $p < 7.6 \times 10^{-9}$; Fisher's exact test). Many of the changes involve increased expression of immediate-early response genes, such as *cFos*, *JunB*, *Egr1*, and *Arc* (Table S3), which is a hallmark of activity-dependent responses (Ebert and Greenberg, 2013). qRT-PCR assays confirmed six out of seven analyzed transcript level changes detected by RNA-seq (Figures 3I and S3G). Moreover, KCl depolarization of neurons and treatment with glutamate receptor agonists results in an even stronger induction of activity-dependent genes in the DKO neurons than in wild-type neurons (Figures 3J and S3H). Collectively, these data provide evidence that the eIF4G microexons control translation of synaptic proteins, including NMDA receptors, to impact activity-dependent gene expression patterns. Moreover, because the eIF4G microexons themselves are regulated by neuronal activity (Figures 2E, S2F, and S2G), the results further suggest that their splicing levels are integral to the control of activity-dependent responses in neurons.

Deletion of the *Eif4g1* Microexon Results in Social Behavior, Learning, and Memory Deficits

To investigate the function of the eIF4G1 and eIF4G3 microexons *in vivo*, we used CRISPR-Cas9 editing to generate mice with each microexon individually deleted (ΔMIC). We crossed heterozygous $Eif4g1^{+/\Delta MIC}$ or $Eif4g3^{+/\Delta MIC}$ animals to generate mice homozygously deleted for each microexon ($Eif4g1^{\Delta MIC/\Delta MIC}$ or $Eif4g3^{\Delta MIC/\Delta MIC}$; Figure 4A). PCR and Sanger sequencing confirmed successful deletions (Figure S4A; data not shown). Both homozygous deletion strains are born with expected Mendelian ratios and do not display obvious morphological phenotypes. For the rest of the study, we focused on the $Eif4g1^{\Delta MIC/\Delta MIC}$ mice, because $Eif4g3^{\Delta MIC/\Delta MIC}$ mice do not display obvious behavioral phenotypes (data not shown). This may be due to the reduced (~2-fold) levels of Eif4g3 relative to Eif4g1 expression or because eIF4G3 may have a greater degree of functional redundancy than eIF4G1.

$Eif4g1^{\Delta MIC/\Delta MIC}$ mice have normal weight, motor coordination, locomotion, habituation, anxiety, aggression, hearing, and response to light stimuli (Figures S4B–S4I). However, they display social behavior abnormalities in the three-chamber apparatus. In this apparatus, wild-type mice generally display a preference for unfamiliar mice over an inanimate object (social preference test) or unfamiliar over familiar mice (social novelty test). $Eif4g1^{\Delta MIC/\Delta MIC}$ mice do not display an appreciable difference with wild-type mice in the social preference test (Figure S4J). However, in contrast to wild-type mice, they lack a social preference in the novelty test (Figures 4B and S4K). Moreover, using the reciprocal interaction test for sociability, which measures the amount of time a mouse spends interacting with an age- and sex-matched mouse of the same genotype, the $Eif4g1^{\Delta MIC/\Delta MIC}$ mice interact significantly less often than do wild-type mice ($p < 0.0384$; two-tailed t test; Figure 4C). Taken together with the finding that the EIF4G1 microexon is among the most strongly skipped in the brains of ASD individuals (Figure S2J), these results suggest that its misregulation may contribute to behavioral phenotypes associated with autism in humans.

Western blotting analysis of synaptosomal preparations from the brains of $Eif4g1^{\Delta MIC/\Delta MIC}$ mice demonstrates that deletion of the *Eif4g1* microexon increases the expression of critical synaptic proteins, including GluN1 (Figure 4D), thus confirming *in vivo* the results from analyzing cultured DKO neurons (Figures 3E and 3F). Given the importance of GluN1 in the control of synaptic plasticity, we investigated whether the $Eif4g1^{\Delta MIC/\Delta MIC}$ mice display altered learning and memory. Notably, the mutant mice have impaired episodic memory, as measured by the contextual fear-conditioning test, which associates a training (environmental) context with a foot shock stimulus and requires both hippocampal- and amygdala-dependent memory formation (Figure 4E; $p < 0.01$; two-way ANOVA). However, no appreciable difference is observed between $Eif4g1^{\Delta MIC/\Delta MIC}$ and wild-type mice when assessing solely amygdala-dependent cued fear conditioning, a test that associates the foot shock with an auditory stimulus, regardless of environment (Figure 4E). These data strongly suggest that mice deficient of the eIF4G1 microexon have impaired hippocampal memory consolidation.

eIF4G1 Microexon Controls Synaptic Transmission and Plasticity

Memory formation involves activity-dependent changes in the strength of specific synaptic connections. Newly acquired memory is temporarily stored in hippocampal circuits by activity-dependent strengthening of individual synapses through processes known as hippocampal long-term potentiation (LTP). Although long-lasting forms of LTP are dependent on new protein synthesis (Costa-Mattioli et al., 2009), activity-dependent mechanisms that serve to maintain long-term synaptic connectivity remain poorly understood. We therefore investigated whether the eIF4G1 microexon controls synaptic function and plasticity in hippocampal slices from wild-type and $Eif4g1^{\Delta MIC/\Delta MIC}$ littermates. Whole cell voltage-clamp recording in CA1 hippocampal neurons reveals a significant increase in the amplitude of spontaneous inhibitory postsynaptic currents (sIPSCs) compared to wild-type neurons (Figure 5A; $p < 1 \times 10^{-5}$; Mann-Whitney U test), suggesting that the mutant neurons have increased inhibitory synaptic conductance, as would be expected due to increased expression of inhibitory synaptic proteins, such as Gephyrin and Neuroligin-2 (Figure 4D). This effect is specific to sIPSC amplitude because no appreciable difference in the frequency and amplitude of miniature (m) and spontaneous (s) excitatory postsynaptic currents (EPSCs), or in the

(H) Percentage of activity-dependent genes differentially expressed in DKO neurons (observed) compared to the overall percentage (expected), as detected by RNA-seq analysis. Error bars, SEM; ***$p < 0.001$; Fisher's exact test.

(I and J) qRT-PCR assays monitoring levels of cFos and JunB in WT and DKO mESC-derived neurons at steady state (I) or following depolarization with 55 mM KCl for 30 min (J). Error bars, SD; *$p < 0.05$; **$p < 0.01$; two-tailed t test.

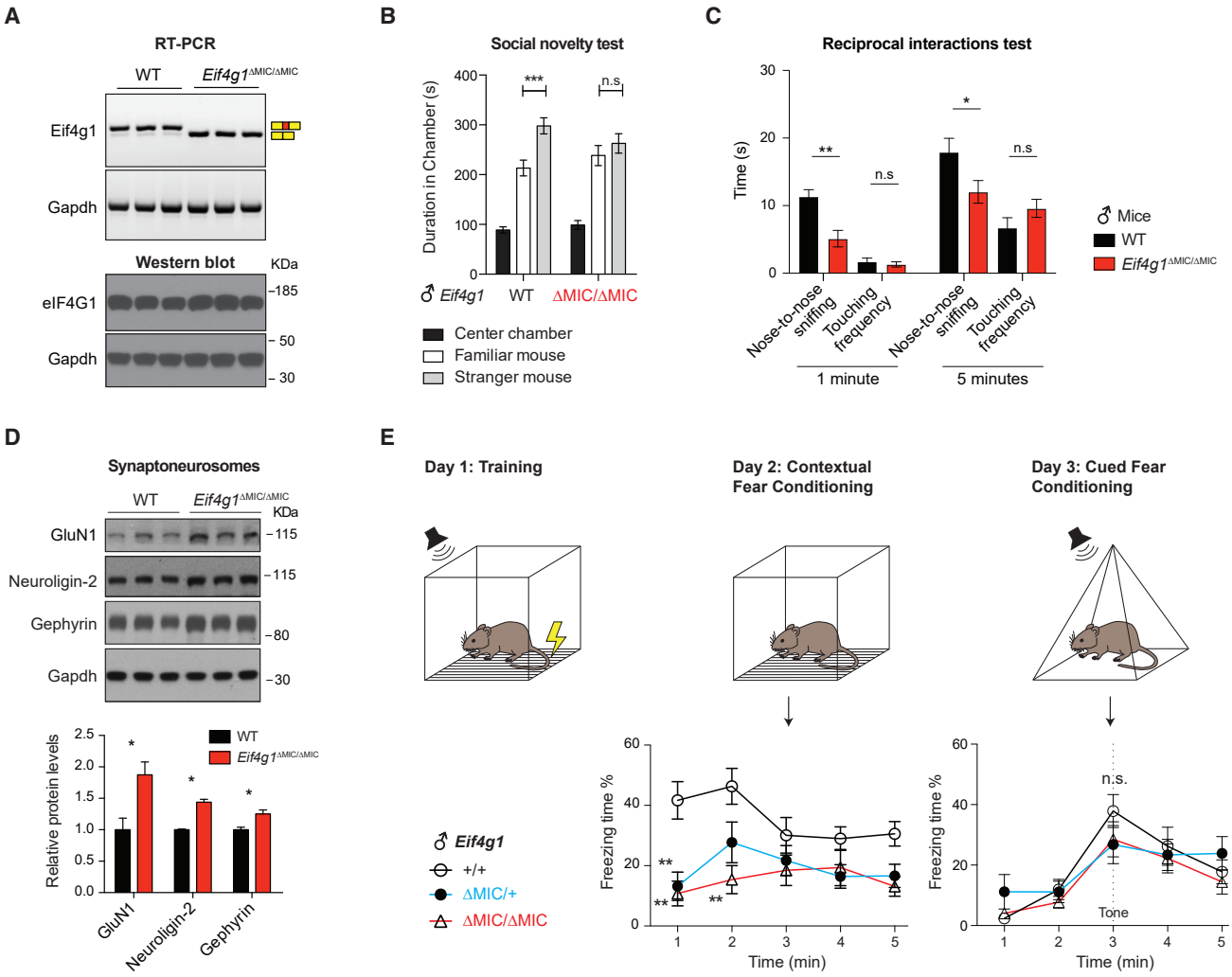

Figure 4. Altered Social Behavior and Impaired Memory in eIF4G1 Microexon-Deficient Mice

(A) RT-PCR (upper) and western blot (lower) monitoring Eif4g1 microexon splicing and eIF4G1 expression from cerebral cortices of P1 WT and *Eif4g1*$^{\Delta MIC/\Delta MIC}$ mice (n = 3).

(B) Three-chamber social novelty test showing the duration of time that WT and *Eif4g1*$^{\Delta MIC/\Delta MIC}$ male mice spent in each chamber; n > 10 mice per genotype. Error bars, SEM; ***p < 0.001; two-way ANOVA and Tukey's post hoc test.

(C) Reciprocal social interaction test showing duration of time for direct nose-to-nose interactions and random touching frequencies. n ≥ 10 male mice per genotype. Error bars, SEM; **p < 0.01; *p < 0.05; two-tailed t test.

(D) Western blots (upper panel) and quantification of relative expression (lower panel) of GluN1, Gephyrin, and Neuroligin-2 protein levels in synaptosomal preparations from WT and *Eif4g1*$^{\Delta MIC/\Delta MIC}$ hippocampal tissues. Gapdh immunoblot is shown to control for loading and recovery. Error bars, SD; *p < 0.05; two-tailed t test.

(E) Schematic representation of fear-conditioning paradigm for testing associative learning and memory (upper panel). Percentage of contextual freezing time of WT, *Eif4g1*$^{+/\Delta MIC}$, or *Eif4g1*$^{\Delta MIC/\Delta MIC}$ mice displayed within a 5-min period 1 day after the acquisition of a noxious stimulus is shown (foot shock; middle panel). Percentage of freezing time of WT, *Eif4g1*$^{+/\Delta MIC}$, or *Eif4g1*$^{\Delta MIC/\Delta MIC}$ mice displayed within a 5-min period, 2 days after the acquisition of a stimulus is shown (foot shock), associated with a tone. The tone was presented during the 3rd min of the test period (right panel). n ≥ 10 mice per genotype; Error bars, SEM; **p < 0.01; two-way ANOVA and Tukey's post hoc test (see Supplemental Information for details).

frequency of m/sIPSCs, is observed (Figures 5A, 5B, S5A, and S5B). In addition, no differences in intrinsic excitability or in resting membrane potential are detected between wild-type and mutant neurons (Figures S5C and S5D). Furthermore, paired-pulse facilitation, a presynaptic form of short-term plasticity, is unchanged, as is the input-output relationship of field excitatory postsynaptic potentials (fEPSPs), which suggests that there are no differences in basal excitatory synaptic transmission between wild-type and *Eif4g1*$^{\Delta MIC/\Delta MIC}$ mice at hippocampal (CA3-CA1 neuron) synapses (Figures 5C and S5E).

We then asked whether the eIF4G1 microexon impacts activity-dependent changes in CA3-CA1 synaptic connections. eIF4G1 microexon-deficient neurons display a significant facilitation of LTP after induction with multiple tetani (i.e., 4 × 100 Hz; 1-s

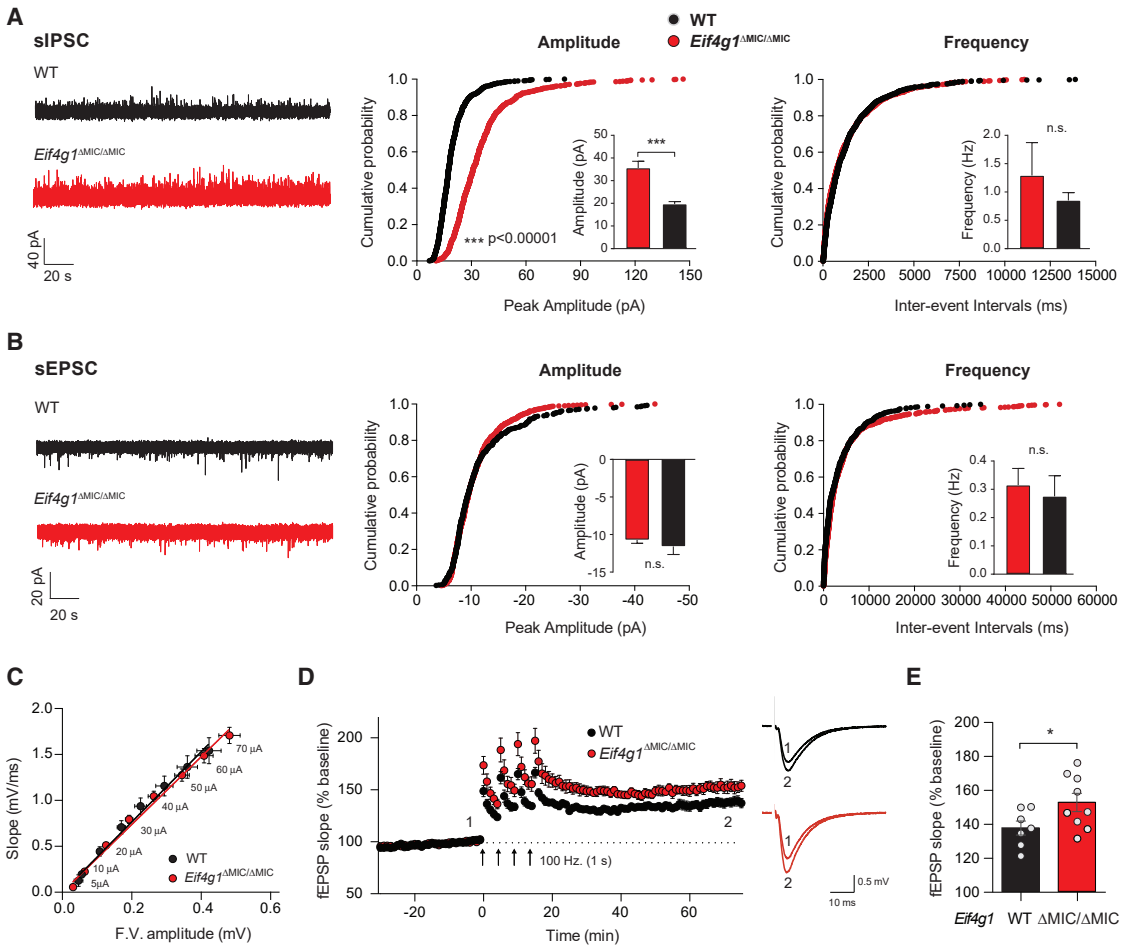

Figure 5. Loss of Eif4g1 Microexon Impacts Synaptic Function and Plasticity

(A and B) Representative traces (left), cumulative distribution, and bar graph plots (right) of sIPSCs (A) and sEPSCs (B) from CA1 hippocampal pyramidal neurons in acute slices from WT and *Eif4g1*$^{\Delta MIC/\Delta MIC}$ mice. *Eif4g1*$^{\Delta MIC/\Delta MIC}$ mice display increased amplitude of inhibitory synaptic transmission. n ≥ 6 slices per genotype; Error bars, SEM; ***p < 0.2 x 10^{-3}; Mann-Whitney U test (bar plots); ***p < 1 x 10^{-5}; Kolmogorov-Smirnov (cumulative probability plots).

(C) Input-output relation of fEPSPs in WT and *Eif4g1*$^{\Delta MIC/\Delta MIC}$ hippocampal slices. n > 18 slices.

(D) LTP induction by four 100-Hz trains (1 s) separated by 5 min each in WT and *Eif4g1*$^{\Delta MIC/\Delta MIC}$ acute hippocampal slices (n ≥ 7 slices; n ≥ 7 mice per genotype). Representative fEPSP recordings from the indicated time points 1 and 2 are shown.

(E) Bar graph showing averaged fEPSP slope (normalized to baseline) between 50 and 60 min post-induction (final tetanus; 100 Hz; 1-s electrical pulse) in WT and *Eif4g1*$^{\Delta MIC/\Delta MIC}$ slices. Error bars, SEM; *p < 0.05; two-tailed t test; n.s., not significant.

electrical pulses) that engage the protein-synthesis-dependent form of LTP (Figures 5D and 5E; p < 0.05; two-tailed t test). These results may be due to increased expression of GluN1 and activity-dependent genes in eIF4G microexon-deficient neurons (Figure 3). Activation of LTP via a milder induction protocol (1 × 100 Hz; 1 s), which leads to protein-synthesis-independent LTP (Costa-Mattioli et al., 2009), fails to induce a significant facilitation of LTP at CA3-CA1 synapses in *Eif4g1*$^{\Delta MIC/\Delta MIC}$ mice (Figures S5F and S5G). Another form of synaptic plasticity dependent on protein synthesis is group 1 metabotropic glutamate receptor (mGluR)-mediated long-term depression (LTD) (Huber et al., 2001). However, mGluR-dependent LTD in *Eif4g1*$^{\Delta MIC/\Delta MIC}$ mice is unaltered (Figures S5H and S5I), indicating that the eIF4G1 microexon regulates specific forms of protein-synthesis-dependent plasticity. Taken together with the behavioral and mass spectrometry data in Figure 3, these results reveal that the eIF4G neuronal microexon functions to regulate the composition of the synaptic proteome to control specific forms of long-lasting synaptic plasticity and, in turn, cognitive functioning.

eIF4G Microexons Promote Associations with Cytoplasmic mRNP Granule Components

To investigate the mechanism by which the eIF4G microexons regulate translation and behavior, we asked whether they encode or overlap amino acid sequence features predictive of functional properties. Both microexons are embedded within eukaryotic-conserved, intrinsically disordered, low-complexity regions identified as "prion-like domains" (Figures 6A and S6A). Prion-like domains have a propensity for phase separation

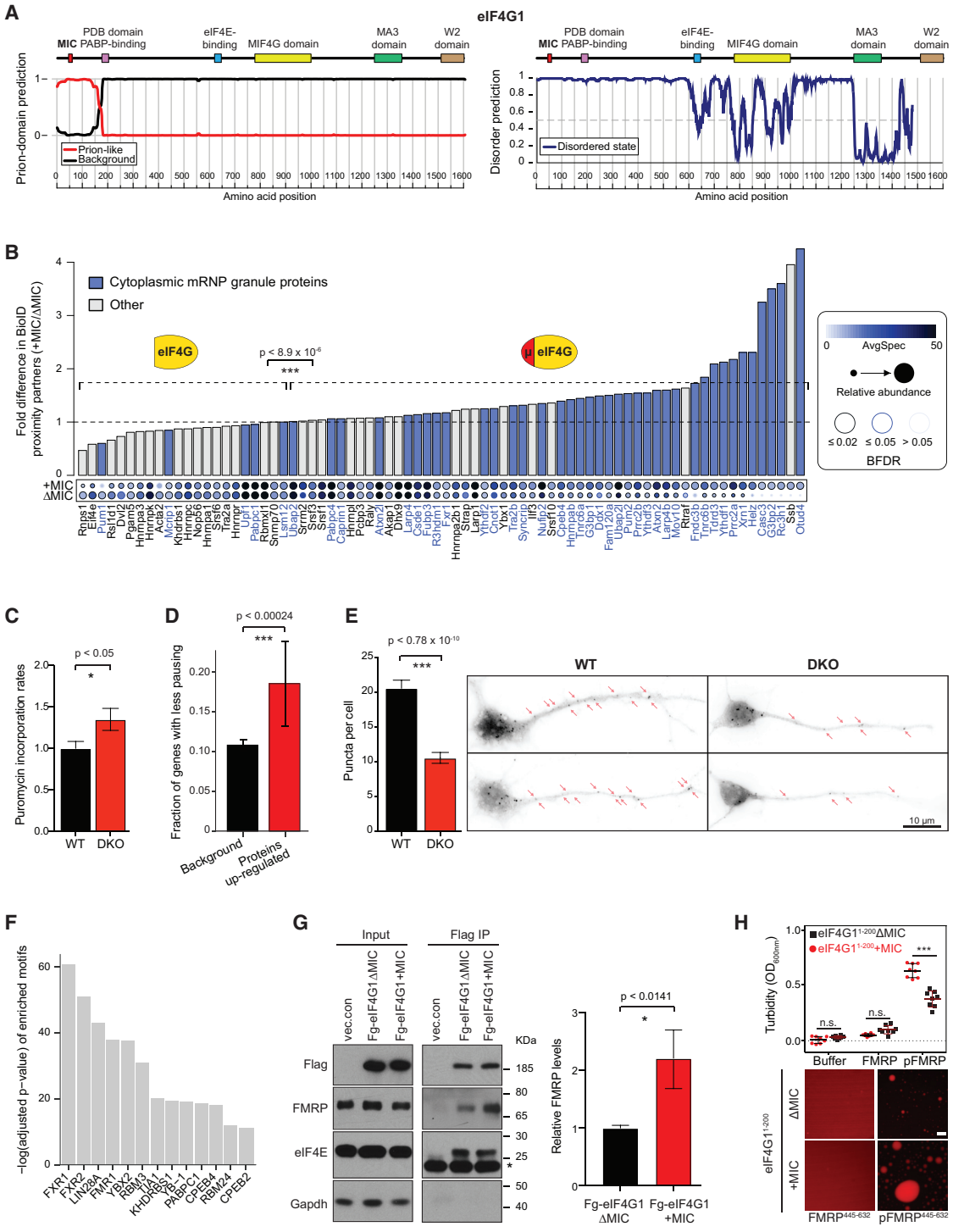

Figure 6. eIF4G Microexon Promotes Interactions with mRNP Cytoplasmic Granule Components and Ribosomal Stalling

(A) Left panel shows predicted prion-like amino acid composition (PLAAC) (Lancaster et al., 2014) for eIF4G1. Right panel shows predicted disordered regions (DISOPRED3) (Jones and Cozzetto, 2015) for human eIF4G1. Known domains and microexon location in eIF4G1 are indicated above the panels. Similar results are shown for eIF4G3 in Figure S6A.

(B) Peptide count ratios from BioID-MS for eIF4G1 and eIF4G1+MIC variants expressed in N2A cells. Proteins previously identified as cytoplasmic mRNP granule components (Youn et al., 2018) are indicated in blue. A significant fold increase in association of granule components with the eIF4G1+MIC relative to the eIF4G1ΔMIC variant is indicated ($p < 8.9 \times 10^{-6}$; Mann-Whitney U test). Dot plot of spectral counts represents the relative abundance of proximal proteins detected for the eIF4G1 splice variants. BFDR, Bayesian false discovery rate.

(legend continued on next page)

in vitro (Banani et al., 2017; Franzmann and Alberti, 2019; Vernon and Forman-Kay, 2019) and contribute to the formation of cellular biomolecular condensates, such as cytoplasmic ribonucleoprotein granules in neurons that function in localized translation and the stabilization of memory formation (Gomes and Shorter, 2019; Li et al., 2013; Mittag and Parker, 2018; Ramaswami et al., 2013; Si and Kandel, 2016). The eIF4G microexon sequences (consensus: GGFRxxQ; Figure 1B) resemble RNA-binding RGG motifs that enhance phase separation via multivalent electrostatic, hydrogen bonding and pi interactions during the formation of granules (Chong et al., 2018; Thandapani et al., 2013). Notably, all of the conserved residues in the microexon sequence contain pi groups (i.e., backbone/side-chain amide, aromatic, and guanidinium) that can contribute to multivalent planar pi-pi stacking interactions with RNA bases, or with similar low-complexity disordered protein regions, to promote phase separation (Nott et al., 2015; Vernon et al., 2018). Thus, inclusion of the microexon is predicted to increase the propensity for phase separation of eIF4G.

To investigate whether the microexons promote phase separation, we generated recombinant proteins comprising the N-terminal disordered region (amino acids 1–200) of eIF4G1, with or without the microexon (eIF4G1$^{1\text{-}200}$+MIC and eIF4G1$^{1\text{-}200}$ΔMIC; Figure S6B). These proteins were analyzed for RNA binding and phase separation *in vitro*. Compared to eIF4G1$^{1\text{-}200}$ΔMIC, the eIF4G1$^{1\text{-}200}$+MIC protein has a modest increase in affinity for RNA, as indicated by fluorescence polarization assays (Figure S6C). Both isoforms phase separate in the presence of RNA, forming liquid droplets (Figure S6D). Notably, the eIF4G1$^{1\text{-}200}$+MIC protein also displays a significantly increased propensity for phase separation compared to eIF4G1$^{1\text{-}200}$ΔMIC, as quantified by turbidity measurements ($p < 0.001$; two-way ANOVA; Figure S6D). These results provide evidence that the eIF4G1 microexon can promote multivalent interactions within phase-separated protein-RNA condensates.

To investigate whether the eIF4G microexons function in the formation of cytoplasmic granules, we employed proximity biotin labeling (i.e., via tagging with the promiscuous biotinylase BirA*), followed by streptavidin capture and mass spectrometry (BioID-MS), to identify microexon-dependent changes in proteins that are proximal to eIF4G1. N2A Flp-In lines expressing N-terminal BirA*-tagged eIF4G1, with and without its microexon (eIF4G1+MIC and eIF4G1ΔMIC), were generated, and captured peptides were quantified for differential enrichment. A significant enrichment for peptides corresponding to proteins with known associations with cytoplasmic mRNP granules (Youn et al., 2018) is observed for the eIF4G1+MIC-proximal interactome, compared to the eIF4G1ΔMIC-proximal interactome ($p < 8.9 \times 10^{-6}$; Mann-Whitney U test; Figure 6B; Table S4). Moreover, the eIF4G1+MIC-proximal interactome comprises a higher fraction of intrinsically disordered amino acid residues relative to the eIF4G1ΔMIC-proximal interactome (Figure S6E), as well as a higher fraction of proteins that contain disordered prion-like domains (Figure S6F). The increased association of eIF4G1+MIC with numerous cytoplasmic granule components, including Fxr1, Ataxin-2, Larp1, and Stau2, was validated by co-immunoprecipitation-western blot analysis using lysates pre-treated with RNase (Figure S6G). Moreover, a comparison of the intracellular localization of mCherry-eIF4G1+MIC and mCherry-eIF4G1ΔMIC proteins reveals that the microexon increases the propensity of eIF4G1 to associate with cytoplasmic foci ($p < 0.0352$; two-way ANOVA; Figure S6H). These data, together with the results from the *in vitro* phase separation assays, are consistent with a role for the eIF4G1 microexon in promoting the formation of neuronal granules.

eIF4G Microexons Promote Associations with FMRP and Ribosome Stalling

An intriguing possibility is that splicing of the eIF4G microexons results in translational repression through their propensity to contribute to the formation of neuronal granules, consistent with known roles for these structures in translational control (Darnell and Richter, 2012; Li et al., 2013; Pimentel and Boccaccio, 2014; Ramaswami et al., 2013). To explore this possibility, we initially investigated the impact of the eIF4G microexons on global protein synthesis rates. Puromycin incorporation into nascent polypeptides reveals a modest but significant increase in the translation rates of the microexon DKO neurons (Figure 6C; $p < 0.05$; two-tailed t test). In contrast, the polysome profiles of wild-type and DKO neurons are essentially indistinguishable, and no appreciable differences are detected in the polysome distributions of transcripts encoding proteins that are upregulated upon deletion of eIF4G microexons (Figure S7A; refer to Figure 3).

Next, we performed ribosome profiling (Ingolia et al., 2011) in wild-type and DKO neurons to assess differences in the

(C) Relative levels of puromycin incorporation in WT and DKO mESC-derived neurons. Error bars, SEM; $p < 0.05$; two-tailed t test.

(D) Bar plots showing the fraction of eIF4G microexon-repressed genes (i.e., with reduced protein expression; see Figure 3C) or background genes that display reduced ribosomal pausing in DKO mESC-derived neurons. Levels of ribosomal pausing were computed with PausePred (Kumari et al., 2018). Error bars, SEM; ***$p < 0.00024$; Fisher's exact test.

(E) *In situ* ribopuromycylation in primary hippocampal neurons to detect stalled ribosomes. Numbers of puncta per neuron (n = 53; right panel) were quantified; error bars, SEM; $p < 0.78 \times 10^{-10}$; Mann-Whitney U test. Images of representative WT and DKO neurons are shown. Red arrows indicate dendritic puncta. Scale bar, 10 μm.

(F) Analysis of motif enrichment in sequences downstream of ribosomal pause sites compared to upstream sequences using CentriMo (Bailey and Machanick, 2012). Proteins with RNA binding sites (Ray et al., 2013) corresponding to motifs enriched with FDR < 0.001 are shown.

(G) Western blot analysis of inputs (left panel) and Flag immunoprecipitates (right panel) from N2A cells transfected with Flag-eIF4G1ΔMIC, Flag-eIF4G1+MIC, or vector control. * indicates Flag antibody light chain. Bar plots depict quantification of FMRP levels from 3 replicates. Error bars, SD; $p < 0.0141$; two-tailed t test.

(H) Turbidity measurements (taken as the optical density at 600 nm) to quantify the phase separation propensity of eIF4G1$^{1\text{-}200}$ ± MIC (30 μM) with FMRP$^{445\text{-}632}$ or pFMRP$^{445\text{-}632}$ (60 μM). Error bars, SEM; ***$p < 0.001$; two-way ANOVA with Bonferroni multiple comparison test. Representative images of eIF4G1$^{1\text{-}200}$ ± MIC (30 μM) and (p)FMRP$^{445\text{-}632}$-FITC (60 μM) droplets are shown. scale bar, 5 μm.

translational engagement of mRNAs. Deep sequencing of ribosome-protected fragments (RPFs) reveals a high degree of reproducibility between replicates (Figure S7B) and the expected three-nucleotide periodicity of the RPF reads (Figure S7C). To compute translational engagement across the transcriptome, we compared the levels of RPF reads relative to the corresponding mRNA reads derived from parallel RNA-seq data. No appreciable differences in overall ribosome occupancy are observed between wild-type and DKO neurons (Figure S7D; Table S5).

We next investigated whether the eIF4G microexons impact ribosome pausing by measuring peaks of RPF reads relative to background densities of reads in the surrounding regions of the corresponding transcripts. Importantly, we detect a global increase in ribosomal stalling across coding sequences in wild-type versus DKO neurons (Figure S7E; $p < 3.09 \times 10^{-6}$; Fisher's exact test; Table S5). Transcripts encoding the synaptic and other proteins in Figure 3C that are translationally repressed by the eIF4G microexons display a significant increase in stalling compared to those of other genes (Figure 6D; $p < 2.4 \times 10^{-4}$; Fisher's exact test). To further test whether the eIF4G microexons induce ribosomal pausing, we performed *in situ* run-off assays in hippocampal neuronal cultures followed by puromycylation (i.e., ribopuromycylation; Graber et al., 2013, 2017). This experiment reveals a significant reduction in stalled ribosomes in the DKO neurons (Figure 6E; $p < 0.78 \times 10^{-10}$; Mann Whitney U test). Collectively, these data strongly suggest that the eIF4G microexons control translation by promoting ribosome stalling.

To further investigate this proposed mechanism, we analyzed the ribosome profiling data for codon or motif enrichment at pausing sites. Consistent with previous observations, we observe increased pausing at stop and arginine codons (Rodnina, 2016) but with no appreciable differences between wild-type and DKO neurons (Figure S7F). However, we detect a strong enrichment for motifs corresponding to known binding sites (Ray et al., 2013) of the FXS-related proteins FXR1, FXR2, and FMRP downstream of pausing sites (Figure 6F; FDR < 0.001). These findings suggest that FMR-related proteins may participate in microexon-dependent ribosome pausing, consistent with our observation of eIF4G microexon-promoted granule component associations involving FMRP and accumulating evidence that cytoplasmic mRNP granules enriched for FMRP are associated with translationally stalled 80S ribosomes (Darnell and Richter, 2012; Darnell et al., 2011; El Fatimy et al., 2016; Graber et al., 2013; Richter and Coller, 2015). Further supporting a mechanistic connection between eIF4G microexons and FMRP, there is a significant enrichment (i.e., odds ratio = 2.6; $p < 0.014$; Fisher's exact test) of FMRP-binding targets among transcripts encoding proteins that are upregulated in the microexon-DKO neurons (Figure S7G). Moreover, transcripts with ribosomal pausing sites in the DKO neurons and those in *Fmr1*-deficient neurons (Liu et al., 2018) significantly overlap ($p < 1.392 \times 10^{-14}$; Fisher's exact test; Figure S7H). Also of note, transcripts that exhibit increased ribosome stalling in the DKO neurons significantly overlap those known to have a dendritic localization (Figure S7I; $p < 1.51 \times 10^{-4}$; Fisher's exact test).

Because eIF4G microexons promote phase separation and the association of numerous cytoplasmic granule components, we asked whether they also enhance interactions with FMRP. Because FMRP is of relatively low abundance and not detected in our BioID-MS analysis, we performed immunoprecipitation of eIF4G1+MIC and eIF4G1ΔMIC splice variants followed by western blot analysis with anti-FMRP antibody. Importantly, the eIF4G1+MIC splice variant displays a 2-fold increased interaction with FMRP that is largely insensitive to RNase treatment (Figures 6G and S6G). Next, to assess whether the eIF4G microexons might directly impact FMRP granule formation, we incubated $eIF4G1^{1\text{-}200}$+MIC and $eIF4G1^{1\text{-}200}$ΔMIC proteins with the recombinant C-terminal disordered region of FMRP (residues 445–632). In this experiment, we compared either phosphorylated (at 8–10 sites) or unphosphorylated forms of $FMRP^{445\text{-}632}$, given previous observations that phospho-FMRP is preferentially associated with translational repression and stalled ribosomes and has a higher propensity to phase separate *in vitro* (Ceman et al., 2003; Tsang et al., 2019). Notably, $eIF4G1^{1\text{-}200}$+MIC has a higher propensity for phase separation with phospho-$FMRP^{445\text{-}632}$ than eIF4G1ΔMIC, as revealed by increased optical density and droplet formation (Figure 6H; $p < 0.001$; two-way ANOVA). Moreover, this property of the $eIF4G1^{1\text{-}200}$+MIC protein is dependent on FMRP phosphorylation because unphosphorylated $FMRP^{445\text{-}632}$ fails to phase separate (Figure 6H).

Taken together, the results provide evidence that the eIF4G microexons promote neuronal granule formation with critical regulators of synaptic translation, including FMRP, and that the resulting interactions likely lead to ribosomal stalling and down-regulation of the translation of synaptic proteins that are critical for proper cognitive functioning (Figure 7).

DISCUSSION

Altered splicing and translational control have emerged as recurring mechanisms underlying ASD and associated neurological disorders (Iakoucheva et al., 2019; Quesnel-Vallières et al., 2019), yet how these two layers of regulation impact each other to control cognitive functioning has not been previously determined. In this study, we show that vertebrate-conserved, neuronal microexons in eIF4G1 and eIF4G3 control the translation of critical synaptic proteins and cognitive functioning. We further provide evidence that the eIF4G microexons normally repress protein synthesis by promoting multivalent interactions with cytoplasmic mRNP components, including the fragile X-linked translation regulator FMRP, that are associated with ribosome stalling. Importantly, the microexons respond to—and elicit—activity-dependent changes in neurons, such that their skipping triggers increased synaptic protein expression and consequent changes in neuronal plasticity, social behavior, as well as learning and memory. Intriguingly, the microexons control the expression and associated functions of key excitatory (e.g., GluN1) and inhibitory (e.g., Gephyrin) synaptic proteins. The altered magnitude of LTP in the $Eif4g1^{\Delta MIC/\Delta MIC}$ mice suggests that skipping of a single microexon can control the expression of proteins required for synaptic plasticity at excitatory synapses. These results thus reveal a unique mechanism through which alternative splicing and translation are coupled to control higher-order cognitive functioning.

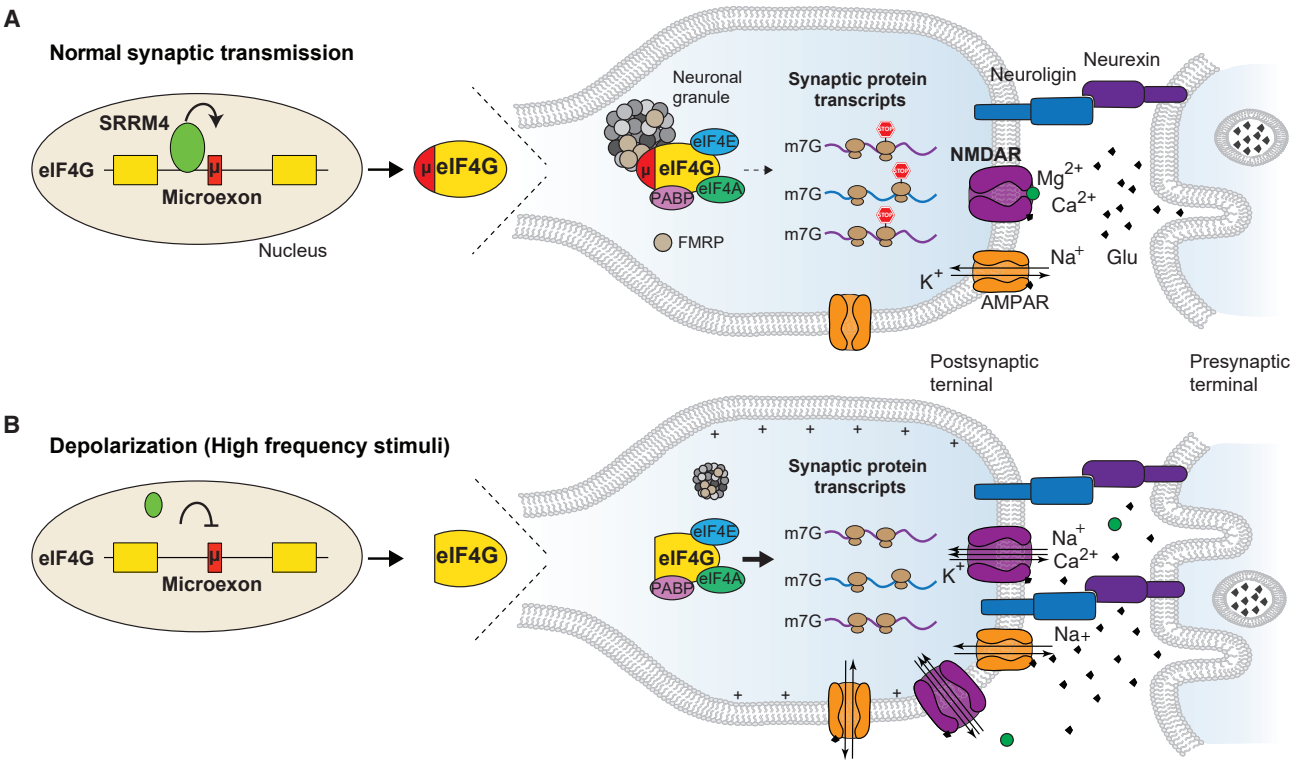

Figure 7. eIF4G Microexon Controls the Translation of Synaptic Proteins that Impact Synaptic Plasticity and Animal Behavior

(A) Mechanistic model illustrating roles for activity-dependent microexon splicing switches in eIF4G proteins in the control of synaptic translation, plasticity, and behavior. eIF4G microexons promote interactions with multiple cytoplasmic mRNP granule components, including FMRP, resulting in reduced translation through increased ribosome pausing.

(B) Neuronal depolarization induces skipping of eIF4G microexons, resulting in dissociation of cytoplasmic granule components and increased translation of synaptic proteins, which in turn alters synaptic transmission and cognitive function. Disruption of eIF4G microexon splicing, which is frequently detected in individuals with ASD, is thus expected to contribute to cognitive impairment by exacerbating neuronal activity-dependent translation outputs.

Our results further highlight a role of alternative splicing in controlling the phase separation propensities of proteins, with associated functional consequences. In particular, our data suggest that the eIF4G microexons impact translation by modulating the propensity of eIF4G to associate and coalesce with components of neuronal granules, including FMRP, in a manner that stalls ribosome elongation on synaptic protein transcripts. Consistent with this proposed mechanism, previous studies have shown that eIF4G associates with FMRP neuronal granules, which contain polyribosomes and multiple additional components identified in our BioID analysis (El Fatimy et al., 2016; Knowles et al., 1996) that have been linked to ribosomal pausing (Ceman et al., 2003; Darnell et al., 2011; Graber et al., 2013; Pimentel and Boccaccio, 2014). Interestingly, despite decreased ribosomal pausing and elevated puromycin incorporation in the *Eif4g1/3* microexon DKO neurons, we did not detect a substantial shift in polysome profiles or overall differences in ribosome occupancy (Figure S7). This suggests that the eIF4G microexons not only induce ribosomal stalling but may also prevent new rounds of translation initiation, which also has been reported to occur in neuronal granules (Graber et al., 2013, 2017; Pimentel and Boccaccio, 2014). Also noteworthy in this regard is that LARP1, which is a cytoplasmic granule component that prevents cap-dependent translation initiation (Fonseca et al., 2015; Lahr et al., 2017; Wilbertz et al., 2019), additionally displays a preferential interaction with the microexon containing eIF4G isoforms (Figures 6B and S6G). Thus, the microexon-promoted associations of multiple granule components likely regulate translation of synaptic protein expression.

Neuronal microexons are significantly enriched for activity-responsive regulation compared to longer brain-specific alternative exons (Quesnel-Vallières et al., 2016), and specific functions for these exons are beginning to emerge. These include roles in chromatin regulation and transcription (e.g., Kdm1a and Mef2c; Rusconi et al., 2017; Zhu et al., 2005), neurite formation (e.g., Unc13b and protrudin; Ohnishi et al., 2014, 2017; Quesnel-Vallières et al., 2015) and animal behavior (Kdm1a and Cpeb4; Parras et al., 2018; Rusconi et al., 2016; Wang et al., 2015). Notably, a recent report has provided evidence that the microexon in Cpeb4 preferentially controls deadenylation and the expression of genes enriched in ASD-risk alleles, and altered ratios of expression of the corresponding Cpeb4 splice variants were associated with ASD-like phenotypes in mice (Parras et al., 2018). Although the mechanism by which the CPEB4 microexon affects translation is not known, like the eIF4G microexon, we observe that it is regulated by Srrm4 (Figures S7J and S7K;

Quesnel-Vallières et al., 2015). Interestingly, CPEB family proteins also have prion-like disordered domains that promote phase separation, and prion-like states of these proteins have been linked to memory stabilization (Si and Kandel, 2016). Taken together with our findings, it is apparent that the wider network of SRRM4-regulated neuronal microexons functions in the activity-dependent remodeling of the neuronal proteome to control animal behavior.

Although misregulation of Srrm4-dependent microexons has been detected in 30% of analyzed ASD patients with idiopathic forms of ASD (Irimia et al., 2014), our findings have intriguing links with FXS. In particular, altered translational control of synaptic proteins as a consequence of eIF4G microexon skipping appears to occur through a mechanism related to that of disruption of the FMRP protein in FXS. It is worth noting, however, that, although the knockout of a single microexon in *Eif4g1* in the present study results in social behavior and cognitive defects, it is probable that the more subtle perturbation of the splicing of this and many additional microexons controlled by Srrm4 collectively contribute to ASD-associated phenotypes. As such, defining the specific functions of additional microexons controlled by Srrm4 represents an important goal of future research. Our results further highlight the potential of modulating Srrm4 and its target microexons as a possible future therapeutic strategy for ASD and related disorders.

STAR★METHODS

Detailed methods are provided in the online version of this paper and include the following:

- KEY RESOURCES TABLE
- LEAD CONTACT AND MATERIALS AVAILABILITY
- EXPERIMENTAL MODEL AND SUBJECT DETAILS
  - Cell culture
  - *In vitro* neuronal differentiation
  - Primary neuronal culture
  - *In vivo* mouse studies
  - Housing and husbandry conditions for experimental animals
- METHOD DETAILS
  - siRNA and plasmid transfections
  - Polysome profiling
  - RNA extraction and RT-PCR assays
  - Quantitative RT-PCR
  - Ribopuromycylation
  - Fluorescence microscopy
  - Co-immunoprecipitation experiments
  - Puromycin labeling
  - Preparation of synaptoneurosomal fractions
  - Immunoblotting
  - Individual-nucleotide Resolution Cross-linking and Immunoprecipitation (iCLIP-Seq)
  - CRISPR/Cas9-directed deletion of Eif4g microexons in CGR8 cells
  - Quantitative proteomics
  - RNA sequencing
  - Ribosome profiling
  - Generation of a stable N2A Flp-In rtTA3 cell lines
  - BioID Sample Preparation for MS
  - BioID mass spectrometry data acquisition
  - Protein phase separation analysis
  - *Eif4g1* and *Eif4g3* microexon deletion mouse lines
  - Brain slice preparation and electrophysiological recordings
  - Spontaneous synaptic transmission recordings
  - Behavioral tests
- QUANTIFICATION AND STATISTICAL ANALYSIS
  - Identification of conserved tissue-specific translation factors
  - PsychENCODE data analysis
  - Computational detection of prion-like and intrinsically disordered regions in eIF4G proteins
  - Quantitative proteomics data analysis
  - Functional enrichment analysis
  - BioID mass spectrometry data analysis
  - BioID data visualization
  - iCLIP-Seq analysis
  - RNA sequencing and ribosome profiling data analysis
  - Overlap of paused genes in Eif4g DKO and *Fmr1* KO neurons
  - Motif enrichment in Eif4g DKO paused genes
  - Quantification of stalled ribosomes from micrographs
  - Foci Quantification
  - Statistics for behavioral testing
- DATA AND CODE AVAILABILITY

SUPPLEMENTAL INFORMATION

Supplemental Information can be found online at https://doi.org/10.1016/j.molcel.2020.01.006.

ACKNOWLEDGMENTS

The authors gratefully acknowledge Jonathan Warner, a giant in the field of ribosome biosynthesis who sadly passed away in September, for inspiring discussions. M. Aregger and A. Nagpal are thanked for helpful comments on the manuscript. D. Torti, T. Durbic, and G. O'Hanlon in the Donnelly Sequencing Centre are gratefully acknowledged for generating RNA-seq data and L. Nutter in The Centre for Phenogenomics (TCP) for assistance with generating mutant mouse strains. We also thank J. Rai for assistance with molecular biology experiments; M. Palandra for assistance with biophysical experiments; R. Vernon for phase separation prediction insights; C. Ouzounis for protein sequence analysis; I. Voineagu for sharing RNA-Seq data; A. Leonelli and C. Dalrymple for mouse husbandry; L. Kelsey, Z. Berberovic, and A. Flenniken for performing ABR and EGR tests; Z. Dargaei and J. Pressey for contributions to the electrophysiology experiments; and A. Au, K. Meier-Ross, and K. Szederkenyi for assistance with microscopy experiments. T.G.-P. was supported by postdoctoral fellowships from EMBO, OIRM, and CIHR; R.J.W. by CIHR Postdoctoral, Marie Curie IOF, and Scrimshaw Foundation fellowships; B.T. by a CIHR Vanier Scholarship; and S.Z. by a Mitacs Elevate postdoctoral fellowship. This research was funded by grants from the Canadian Institutes of Health Research (B.J.B., S.P.C., A.-C.G., M.A.W., J.D.F.-K., and G.L.C.), Simon's Foundation (B.J.B.), Canada First Research Excellence Fund Medicine by Design Program (B.J.B.), Canada Foundation for Innovation and Genome Canada (A.-C.G. and others), European Research Council (ERC) and the Spanish Ministry of Economy (M.I.), Brain Canada (G.L.C.), Camille Dan Chair Mt. Sinai Hospital (S.P.C.), and Canada Research Chairs Tier I (J.D.F.-K., S.P.C. and A.-C.G.). B.J.B. holds the Banbury Chair in Medical Research at the University of Toronto.

AUTHOR CONTRIBUTIONS

T.G.-P. performed molecular and cellular characterization of the regulation and function of microexons, with contributions from S.F., T.H., and E.S.; R.J.W., U.B., T.G.-P., and M.I. performed analyses of RNA-seq, Ribo-seq, and CLIP-seq; B.T. and J.D.F.-K. generated and analyzed *in vitro* RNA binding and phase separation data; J.P. analyzed microexon regulatory conservation in zebrafish; S.Z., J.R., T.G.-P., R.J.W., U.B., S.M., and A.-C.G. generated and analyzed MS data; E.W.S., X.L., J.G., G.L.C., and M.A.W. generated and analyzed electrophysiology data; and R.N., T.G.-P., M.Q.-V., and S.P.C. performed and analyzed *in vivo* phenotypic data. N.S. contributed critical reagents and insights. T.G.-P., S.P.C., and B.J.B. designed the study with input from other authors. T.G.-P. and B.J.B. wrote the manuscript with input from other authors.

DECLARATION OF INTERESTS

The authors declare no competing interests.

Received: January 21, 2019
Revised: August 15, 2019
Accepted: January 2, 2020
Published: January 29, 2020

REFERENCES

Anders, S., and Huber, W. (2010). Differential expression analysis for sequence count data. Genome Biol. *11*, R106.

Anderson, W.W., and Collingridge, G.L. (2007). Capabilities of the WinLTP data acquisition program extending beyond basic LTP experimental functions. J. Neurosci. Methods *162*, 346–356.

Auerbach, B.D., Osterweil, E.K., and Bear, M.F. (2011). Mutations causing syndromic autism define an axis of synaptic pathophysiology. Nature *480*, 63–68.

Bagni, C., and Zukin, R.S. (2019). A synaptic perspective of fragile X syndrome and autism spectrum disorders. Neuron *101*, 1070–1088.

Bailey, T.L., and Machanick, P. (2012). Inferring direct DNA binding from ChIP-seq. Nucleic Acids Res. *40*, e128.

Bakker, C.E., Verheij, C., Willemsen, R., van der Helm, R., Oerlemans, F., Vermey, M., Bygrave, A., Hoogeveen, A., Oostra, B.A., Reyniers, E., et al.; The Dutch-Belgian Fragile X Consortium (1994). Fmr1 knockout mice: a model to study fragile X mental retardation. Cell *78*, 23–33.

Bakthavachalu, B., Huelsmeier, J., Sudhakaran, I.P., Hillebrand, J., Singh, A., Petrauskas, A., Thiagarajan, D., Sankaranarayanan, M., Mizoue, L., Anderson, E.N., et al. (2018). RNP-granule assembly via ataxin-2 disordered domains is required for long-term memory and neurodegeneration. Neuron *98*, 754–766.e4.

Banani, S.F., Lee, H.O., Hyman, A.A., and Rosen, M.K. (2017). Biomolecular condensates: organizers of cellular biochemistry. Nat. Rev. Mol. Cell Biol. *18*, 285–298.

Baralle, F.E., and Giudice, J. (2017). Alternative splicing as a regulator of development and tissue identity. Nat. Rev. Mol. Cell Biol. *18*, 437–451.

Barbosa-Morais, N.L., Irimia, M., Pan, Q., Xiong, H.Y., Gueroussov, S., Lee, L.J., Slobodeniuc, V., Kutter, C., Watt, S., Colak, R., et al. (2012). The evolutionary landscape of alternative splicing in vertebrate species. Science *338*, 1587–1593.

Bolger, A.M., Lohse, M., and Usadel, B. (2014). Trimmomatic: a flexible trimmer for Illumina sequence data. Bioinformatics *30*, 2114–2120.

Borrie, S.C., Brems, H., Legius, E., and Bagni, C. (2017). Cognitive dysfunctions in intellectual disabilities: the contributions of the Ras-MAPK and PI3K-AKT-mTOR pathways. Annu. Rev. Genomics Hum. Genet. *18*, 115–142.

Bray, N.L., Pimentel, H., Melsted, P., and Pachter, L. (2016). Near-optimal probabilistic RNA-seq quantification. Nat. Biotechnol. *34*, 525–527.

C Yuen, R.K., Merico, D., Bookman, M., L Howe, J., Thiruvahindrapuram, B., Patel, R.V., Whitney, J., Deflaux, N., Bingham, J., Wang, Z., et al. (2017). Whole genome sequencing resource identifies 18 new candidate genes for autism spectrum disorder. Nat. Neurosci. *20*, 602–611.

Cajigas, I.J., Tushev, G., Will, T.J., tom Dieck, S., Fuerst, N., and Schuman, E.M. (2012). The local transcriptome in the synaptic neuropil revealed by deep sequencing and high-resolution imaging. Neuron *74*, 453–466.

Calarco, J.A., Superina, S., O'Hanlon, D., Gabut, M., Raj, B., Pan, Q., Skalska, U., Clarke, L., Gelinas, D., van der Kooy, D., et al. (2009). Regulation of vertebrate nervous system alternative splicing and development by an SR-related protein. Cell *138*, 898–910.

Ceman, S., O'Donnell, W.T., Reed, M., Patton, S., Pohl, J., and Warren, S.T. (2003). Phosphorylation influences the translation state of FMRP-associated polyribosomes. Hum. Mol. Genet. *12*, 3295–3305.

Chong, P.A., Vernon, R.M., and Forman-Kay, J.D. (2018). RGG/RG motif regions in RNA binding and phase separation. J. Mol. Biol. *430*, 4650–4665.

Costa-Mattioli, M., Sossin, W.S., Klann, E., and Sonenberg, N. (2009). Translational control of long-lasting synaptic plasticity and memory. Neuron *61*, 10–26.

Darnell, J.C., and Richter, J.D. (2012). Cytoplasmic RNA-binding proteins and the control of complex brain function. Cold Spring Harb. Perspect. Biol. *4*, a012344.

Darnell, J.C., Van Driesche, S.J., Zhang, C., Hung, K.Y.S., Mele, A., Fraser, C.E., Stone, E.F., Chen, C., Fak, J.J., Chi, S.W., et al. (2011). FMRP stalls ribosomal translocation on mRNAs linked to synaptic function and autism. Cell *146*, 247–261.

De Rubeis, S., He, X., Goldberg, A.P., Poultney, C.S., Samocha, K., Cicek, A.E., Kou, Y., Liu, L., Fromer, M., Walker, S., et al.; DDD Study; Homozygosity Mapping Collaborative for Autism; UK10K Consortium (2014). Synaptic, transcriptional and chromatin genes disrupted in autism. Nature *515*, 209–215.

Dergai, M., Tsyba, L., Dergai, O., Zlatskii, I., Skrypkina, I., Kovalenko, V., and Rynditch, A. (2010). Microexon-based regulation of ITSN1 and Src SH3 domains specificity relies on introduction of charged amino acids into the interaction interface. Biochem. Biophys. Res. Commun. *399*, 307–312.

Deutsch, E.W., Mendoza, L., Shteynberg, D., Farrah, T., Lam, H., Tasman, N., Sun, Z., Nilsson, E., Pratt, B., Prazen, B., et al. (2010). A guided tour of the Trans-Proteomic Pipeline. Proteomics *10*, 1150–1159.

Ebert, D.H., and Greenberg, M.E. (2013). Activity-dependent neuronal signalling and autism spectrum disorder. Nature *493*, 327–337.

Ehninger, D., Han, S., Shilyansky, C., Zhou, Y., Li, W., Kwiatkowski, D.J., Ramesh, V., and Silva, A.J. (2008). Reversal of learning deficits in a Tsc2+/- mouse model of tuberous sclerosis. Nat. Med. *14*, 843–848.

El Fatimy, R., Davidovic, L., Tremblay, S., Jaglin, X., Dury, A., Robert, C., De Koninck, P., and Khandjian, E.W. (2016). Tracking the fragile X mental retardation protein in a highly ordered neuronal ribonucleoparticles population: a link between stalled polyribosomes and RNA granules. PLoS Genet. *12*, e1006192.

Feng, Y., Zhang, F., Lokey, L.K., Chastain, J.L., Lakkis, L., Eberhart, D., and Warren, S.T. (1995). Translational suppression by trinucleotide repeat expansion at FMR1. Science *268*, 731–734.

Fonseca, B.D., Zakaria, C., Jia, J.-J., Graber, T.E., Svitkin, Y., Tahmasebi, S., Healy, D., Hoang, H.-D., Jensen, J.M., Diao, I.T., et al. (2015). La-related protein 1 (LARP1) represses terminal oligopyrimidine (TOP) mRNA translation downstream of mTOR complex 1 (mTORC1). J. Biol. Chem. *290*, 15996–16020.

Franzmann, T.M., and Alberti, S. (2019). Prion-like low-complexity sequences: Key regulators of protein solubility and phase behavior. J. Biol. Chem. *294*, 7128–7136.

Gandal, M.J., Zhang, P., Hadjimichael, E., Walker, R.L., Chen, C., Liu, S., Won, H., van Bakel, H., Varghese, M., Wang, Y., et al. (2018). Transcriptome-wide isoform-level dysregulation in ASD, schizophrenia, and bipolar disorder. Science *362*, eaat8127.

Gertsenstein, M., and Nutter, L.M.J. (2018). Engineering point mutant and epitope-tagged alleles in mice using Cas9 RNA-guided nuclease. Curr. Protoc. Mouse Biol. *8*, 28–53.

Gingras, A.C., Raught, B., and Sonenberg, N. (1999). eIF4 initiation factors: effectors of mRNA recruitment to ribosomes and regulators of translation. Annu. Rev. Biochem. *68*, 913–963.

Gkogkas, C.G., Khoutorsky, A., Ran, I., Rampakakis, E., Nevarko, T., Weatherill, D.B., Vasuta, C., Yee, S., Truitt, M., Dallaire, P., et al. (2013). Autism-related deficits via dysregulated eIF4E-dependent translational control. Nature *493*, 371–377.

Gomes, E., and Shorter, J. (2019). The molecular language of membraneless organelles. J. Biol. Chem. *294*, 7115–7127.

Gonatopoulos-Pournatzis, T., Wu, M., Braunschweig, U., Roth, J., Han, H., Best, A.J., Raj, B., Aregger, M., O'Hanlon, D., Ellis, J.D., et al. (2018). Genome-wide CRISPR-Cas9 interrogation of splicing networks reveals a mechanism for recognition of autism-misregulated neuronal microexons. Mol. Cell *72*, 510–524.e12.

Graber, T.E., Hébert-Seropian, S., Khoutorsky, A., David, A., Yewdell, J.W., Lacaille, J.-C., and Sossin, W.S. (2013). Reactivation of stalled polyribosomes in synaptic plasticity. Proc. Natl. Acad. Sci. USA *110*, 16205–16210.

Graber, T.E., Freemantle, E., Anadolu, M.N., Hébert-Seropian, S., MacAdam, R.L., Shin, U., Hoang, H.-D., Alain, T., Lacaille, J.-C., and Sossin, W.S. (2017). UPF1 governs synaptic plasticity through association with a STAU2 RNA granule. J. Neurosci. *37*, 9116–9131.

Gueroussov, S., Gonatopoulos-Pournatzis, T., Irimia, M., Raj, B., Lin, Z.-Y., Gingras, A.-C., and Blencowe, B.J. (2015). An alternative splicing event amplifies evolutionary differences between vertebrates. Science *349*, 868–873.

Gupta, V., and Warner, J.R. (2014). Ribosome-omics of the human ribosome. RNA *20*, 1004–1013.

Han, H., Braunschweig, U., Gonatopoulos-Pournatzis, T., Weatheritt, R.J., Hirsch, C.L., Ha, K.C.H., Radovani, E., Nabeel-Shah, S., Sterne-Weiler, T., Wang, J., et al. (2017). Multilayered control of alternative splicing regulatory networks by transcription factors. Mol. Cell *65*, 539–553.e7.

Holt, C.E., and Schuman, E.M. (2013). The central dogma decentralized: new perspectives on RNA function and local translation in neurons. Neuron *80*, 648–657.

Hubbard, K.S., Gut, I.M., Lyman, M.E., and McNutt, P.M. (2013). Longitudinal RNA sequencing of the deep transcriptome during neurogenesis of cortical glutamatergic neurons from murine ESCs. F1000Res. *2*, 35.

Huber, K.M., Roder, J.C., and Bear, M.F. (2001). Chemical induction of mGluR5- and protein synthesis–dependent long-term depression in hippocampal area CA1. J. Neurophysiol. *86*, 321–325.

Huber, K.M., Gallagher, S.M., Warren, S.T., and Bear, M.F. (2002). Altered synaptic plasticity in a mouse model of fragile X mental retardation. Proc. Natl. Acad. Sci. USA *99*, 7746–7750.

Huppertz, I., Attig, J., D'Ambrogio, A., Easton, L.E., Sibley, C.R., Sugimoto, Y., Tajnik, M., König, J., and Ule, J. (2014). iCLIP: protein-RNA interactions at nucleotide resolution. Methods *65*, 274–287.

Iakoucheva, L.M., Muotri, A.R., and Sebat, J. (2019). Getting to the cores of autism. Cell *178*, 1287–1298.

Ingolia, N.T., Lareau, L.F., and Weissman, J.S. (2011). Ribosome profiling of mouse embryonic stem cells reveals the complexity and dynamics of mammalian proteomes. Cell *147*, 789–802.

Iossifov, I., O'Roak, B.J., Sanders, S.J., Ronemus, M., Krumm, N., Levy, D., Stessman, H.A., Witherspoon, K.T., Vives, L., Patterson, K.E., et al. (2014). The contribution of de novo coding mutations to autism spectrum disorder. Nature *515*, 216–221.

Irimia, M., Weatheritt, R.J., Ellis, J.D., Parikshak, N.N., Gonatopoulos-Pournatzis, T., Babor, M., Quesnel-Vallières, M., Tapial, J., Raj, B., O'Hanlon, D., et al. (2014). A highly conserved program of neuronal microexons is misregulated in autistic brains. Cell *159*, 1511–1523.

Isserlin, R., Merico, D., Voisin, V., and Bader, G.D. (2014). Enrichment Map - a Cytoscape app to visualize and explore OMICs pathway enrichment results. F1000Res. *3*, 141.

Jones, D.T., and Cozzetto, D. (2015). DISOPRED3: precise disordered region predictions with annotated protein-binding activity. Bioinformatics *31*, 857–863.

Jung, H., Gkogkas, C.G., Sonenberg, N., and Holt, C.E. (2014). Remote control of gene function by local translation. Cell *157*, 26–40.

Knight, J.D.R., Choi, H., Gupta, G.D., Pelletier, L., Raught, B., Nesvizhskii, A.I., and Gingras, A.-C. (2017). ProHits-viz: a suite of web tools for visualizing interaction proteomics data. Nat. Methods *14*, 645–646.

Knowles, R.B., Sabry, J.H., Martone, M.E., Deerinck, T.J., Ellisman, M.H., Bassell, G.J., and Kosik, K.S. (1996). Translocation of RNA granules in living neurons. J. Neurosci. *16*, 7812–7820.

Kumari, R., Michel, A.M., and Baranov, P.V. (2018). PausePred and Rfeet: webtools for inferring ribosome pauses and visualizing footprint density from ribosome profiling data. RNA *24*, 1297–1304.

Lahr, R.M., Fonseca, B.D., Ciotti, G.E., Al-Ashtal, H.A., Jia, J.-J., Niklaus, M.R., Blagden, S.P., Alain, T., and Berman, A.J. (2017). La-related protein 1 (LARP1) binds the mRNA cap, blocking eIF4F assembly on TOP mRNAs. eLife *6*, e24146.

Lambert, J.-P., Tucholska, M., Go, C., Knight, J.D.R., and Gingras, A.-C. (2015). Proximity biotinylation and affinity purification are complementary approaches for the interactome mapping of chromatin-associated protein complexes. J. Proteomics *118*, 81–94.

Lancaster, A.K., Nutter-Upham, A., Lindquist, S., and King, O.D. (2014). PLAAC: a web and command-line application to identify proteins with prion-like amino acid composition. Bioinformatics *30*, 2501–2502.

Lee, J.-A., Tang, Z.-Z., and Black, D.L. (2009). An inducible change in Fox-1/A2BP1 splicing modulates the alternative splicing of downstream neuronal target exons. Genes Dev. *23*, 2284–2293.

Lee, J.-A., Damianov, A., Lin, C.-H., Fontes, M., Parikshak, N.N., Anderson, E.S., Geschwind, D.H., Black, D.L., and Martin, K.C. (2016). Cytoplasmic Rbfox1 regulates the expression of synaptic and autism-related genes. Neuron *89*, 113–128.

Li, Y.R., King, O.D., Shorter, J., and Gitler, A.D. (2013). Stress granules as crucibles of ALS pathogenesis. J. Cell Biol. *201*, 361–372.

Li, Y.I., Sanchez-Pulido, L., Haerty, W., and Ponting, C.P. (2015). RBFOX and PTBP1 proteins regulate the alternative splicing of micro-exons in human brain transcripts. Genome Res. *25*, 1–13.

Licatalosi, D.D., and Darnell, R.B. (2010). RNA processing and its regulation: global insights into biological networks. Nat. Rev. Genet. *11*, 75–87.

Lim, E.T., Uddin, M., De Rubeis, S., Chan, Y., Kamumbu, A.S., Zhang, X., D'Gama, A.M., Kim, S.N., Hill, R.S., Goldberg, A.P., et al.; Autism Sequencing Consortium (2017). Rates, distribution and implications of postzygotic mosaic mutations in autism spectrum disorder. Nat. Neurosci. *20*, 1217–1224.

Liu, G., Knight, J.D.R., Zhang, J.P., Tsou, C.-C., Wang, J., Lambert, J.-P., Larsen, B., Tyers, M., Raught, B., Bandeira, N., et al. (2016). Data Independent Acquisition analysis in ProHits 4.0. J. Proteomics *149*, 64–68.

Liu, B., Li, Y., Stackpole, E.E., Novak, A., Gao, Y., Zhao, Y., Zhao, X., and Richter, J.D. (2018). Regulatory discrimination of mRNAs by FMRP controls mouse adult neural stem cell differentiation. Proc. Natl. Acad. Sci. USA *115*, E11397–E11405.

Lovci, M.T., Ghanem, D., Marr, H., Arnold, J., Gee, S., Parra, M., Liang, T.Y., Stark, T.J., Gehman, L.T., Hoon, S., et al. (2013). Rbfox proteins regulate alternative mRNA splicing through evolutionarily conserved RNA bridges. Nat. Struct. Mol. Biol. *20*, 1434–1442.

Lucariello, M., Vidal, E., Vidal, S., Saez, M., Roa, L., Huertas, D., Pineda, M., Dalfó, E., Dopazo, J., Jurado, P., et al. (2016). Whole exome sequencing of Rett syndrome-like patients reveals the mutational diversity of the clinical phenotype. Hum. Genet. *135*, 1343–1354.

Maurin, T., Lebrigand, K., Castagnola, S., Paquet, A., Jarjat, M., Popa, A., Grossi, M., Rage, F., and Bardoni, B. (2018). HITS-CLIP in various brain areas reveals new targets and new modalities of RNA binding by fragile X mental retardation protein. Nucleic Acids Res. *46*, 6344–6355.

Merkin, J., Russell, C., Chen, P., and Burge, C.B. (2012). Evolutionary dynamics of gene and isoform regulation in Mammalian tissues. Science *338*, 1593–1599.

Mittag, T., and Parker, R. (2018). Multiple modes of protein-protein interactions promote RNP granule assembly. J. Mol. Biol. *430*, 4636–4649.

Neves-Pereira, M., Müller, B., Massie, D., Williams, J.H.G., O'Brien, P.C.M., Hughes, A., Shen, S.-B., Clair, D.S., and Miedzybrodzka, Z. (2009). Deregulation of EIF4E: a novel mechanism for autism. J. Med. Genet. *46*, 759–765.

Nguyen, L.S., Kim, H.-G., Rosenfeld, J.A., Shen, Y., Gusella, J.F., Lacassie, Y., Layman, L.C., Shaffer, L.G., and Gécz, J. (2013). Contribution of copy number variants involving nonsense-mediated mRNA decay pathway genes to neurodevelopmental disorders. Hum. Mol. Genet. *22*, 1816–1825.

Nott, T.J., Petsalaki, E., Farber, P., Jervis, D., Fussner, E., Plochowietz, A., Craggs, T.D., Bazett-Jones, D.P., Pawson, T., Forman-Kay, J.D., and Baldwin, A.J. (2015). Phase transition of a disordered nuage protein generates environmentally responsive membraneless organelles. Mol. Cell *57*, 936–947.

Nussbacher, J.K., Batra, R., Lagier-Tourenne, C., and Yeo, G.W. (2015). RNA-binding proteins in neurodegeneration: Seq and you shall receive. Trends Neurosci. *38*, 226–236.

Ohnishi, T., Shirane, M., Hashimoto, Y., Saita, S., and Nakayama, K.I. (2014). Identification and characterization of a neuron-specific isoform of protrudin. Genes Cells *19*, 97–111.

Ohnishi, T., Shirane, M., and Nakayama, K.I. (2017). SRRM4-dependent neuron-specific alternative splicing of protrudin transcripts regulates neurite outgrowth. Sci. Rep. *7*, 41130.

Palmer, M.J., Irving, A.J., Seabrook, G.R., Jane, D.E., and Collingridge, G.L. (1997). The group I mGlu receptor agonist DHPG induces a novel form of LTD in the CA1 region of the hippocampus. Neuropharmacology *36*, 1517–1532.

Parras, A., Anta, H., Santos-Galindo, M., Swarup, V., Elorza, A., Nieto-González, J.L., Picó, S., Hernández, I.H., Díaz-Hernández, J.I., Belloc, E., et al. (2018). Autism-like phenotype and risk gene mRNA deadenylation by CPEB4 mis-splicing. Nature *560*, 441–446.

Pimentel, J., and Boccaccio, G.L. (2014). Translation and silencing in RNA granules: a tale of sand grains. Front. Mol. Neurosci. *7*, 68.

Pirooznia, M., Wang, T., Avramopoulos, D., Valle, D., Thomas, G., Huganir, R.L., Goes, F.S., Potash, J.B., and Zandi, P.P. (2012). SynaptomeDB: an ontology-based knowledgebase for synaptic genes. Bioinformatics *28*, 897–899.

Quesnel-Vallières, M., Irimia, M., Cordes, S.P., and Blencowe, B.J. (2015). Essential roles for the splicing regulator nSR100/SRRM4 during nervous system development. Genes Dev. *29*, 746–759.

Quesnel-Vallières, M., Dargaei, Z., Irimia, M., Gonatopoulos-Pournatzis, T., Ip, J.Y., Wu, M., Sterne-Weiler, T., Nakagawa, S., Woodin, M.A., Blencowe, B.J., and Cordes, S.P. (2016). Misregulation of an activity-dependent splicing network as a common mechanism underlying autism spectrum disorders. Mol. Cell *64*, 1023–1034.

Quesnel-Vallières, M., Weatheritt, R.J., Cordes, S.P., and Blencowe, B.J. (2019). Autism spectrum disorder: insights into convergent mechanisms from transcriptomics. Nat. Rev. Genet. *20*, 51–63.

Raj, B., and Blencowe, B.J. (2015). Alternative splicing in the mammalian nervous system: recent insights into mechanisms and functional roles. Neuron *87*, 14–27.

Raj, B., Irimia, M., Braunschweig, U., Sterne-Weiler, T., O'Hanlon, D., Lin, Z.-Y., Chen, G.I., Easton, L.E., Ule, J., Gingras, A.-C., et al. (2014). A global regulatory mechanism for activating an exon network required for neurogenesis. Mol. Cell *56*, 90–103.

Ramaswami, M., Taylor, J.P., and Parker, R. (2013). Altered ribostasis: RNA-protein granules in degenerative disorders. Cell *154*, 727–736.

Ran, F.A., Hsu, P.D., Wright, J., Agarwala, V., Scott, D.A., and Zhang, F. (2013). Genome engineering using the CRISPR-Cas9 system. Nat. Protoc. *8*, 2281–2308.

Ray, D., Kazan, H., Cook, K.B., Weirauch, M.T., Najafabadi, H.S., Li, X., Gueroussov, S., Albu, M., Zheng, H., Yang, A., et al. (2013). A compendium of RNA-binding motifs for decoding gene regulation. Nature *499*, 172–177.

Reimand, J., Arak, T., Adler, P., Kolberg, L., Reisberg, S., Peterson, H., and Vilo, J. (2016). g:Profiler-a web server for functional interpretation of gene lists (2016 update). Nucleic Acids Res. *44* (W1), W83–W89.

Richter, J.D., and Coller, J. (2015). Pausing on polyribosomes: make way for elongation in translational control. Cell *163*, 292–300.

Richter, J.D., Bassell, G.J., and Klann, E. (2015). Dysregulation and restoration of translational homeostasis in fragile X syndrome. Nat. Rev. Neurosci. *16*, 595–605.

Rodnina, M.V. (2016). The ribosome in action: tuning of translational efficiency and protein folding. Protein Sci. *25*, 1390–1406.

Rusconi, F., Grillo, B., Ponzoni, L., Bassani, S., Toffolo, S., Paganini, L., Mallei, A., Braida, D., Passafaro, M., Popoli, M., et al. (2016). LSD1 modulates stress-evoked transcription of immediate early genes and emotional behavior. Proc. Natl. Acad. Sci. *113*, 3651–3656.

Rusconi, F., Grillo, B., Toffolo, E., Mattevi, A., and Battaglioli, E. (2017). NeuroLSD1: splicing-generated epigenetic enhancer of neuroplasticity. Trends Neurosci. *40*, 28–38.

Santini, E., and Klann, E. (2014). Reciprocal signaling between translational control pathways and synaptic proteins in autism spectrum disorders. Sci. Signal. *7*, re10.

Santini, E., Huynh, T.N., MacAskill, A.F., Carter, A.G., Pierre, P., Ruggero, D., Kaphzan, H., and Klann, E. (2013). Exaggerated translation causes synaptic and behavioural aberrations associated with autism. Nature *493*, 411–415.

Scotti, M.M., and Swanson, M.S. (2016). RNA mis-splicing in disease. Nat. Rev. Genet. *17*, 19–32.

Shteynberg, D., Deutsch, E.W., Lam, H., Eng, J.K., Sun, Z., Tasman, N., Mendoza, L., Moritz, R.L., Aebersold, R., and Nesvizhskii, A.I. (2011). iProphet: multi-level integrative analysis of shotgun proteomic data improves peptide and protein identification rates and error estimates. Mol. Cell. Proteomics *10*, M111.007690.

Si, K., and Kandel, E.R. (2016). The role of functional prion-like proteins in the persistence of memory. Cold Spring Harb. Perspect. Biol. *8*, a021774.

Sibley, C.R., Blazquez, L., and Ule, J. (2016). Lessons from non-canonical splicing. Nat. Rev. Genet. *17*, 407–421.

Tapial, J., Ha, K.C.H., Sterne-Weiler, T., Gohr, A., Braunschweig, U., Hermoso-Pulido, A., Quesnel-Vallières, M., Permanyer, J., Sodaei, R., Marquez, Y., et al. (2017). An atlas of alternative splicing profiles and functional associations reveals new regulatory programs and genes that simultaneously express multiple major isoforms. Genome Res. *27*, 1759–1768.

Teo, G., Liu, G., Zhang, J., Nesvizhskii, A.I., Gingras, A.-C., and Choi, H. (2014). SAINTexpress: improvements and additional features in Significance Analysis of INTeractome software. J. Proteomics *100*, 37–43.

Thandapani, P., O'Connor, T.R., Bailey, T.L., and Richard, S. (2013). Defining the RGG/RG motif. Mol. Cell *50*, 613–623.

Toffolo, E., Rusconi, F., Paganini, L., Tortorici, M., Pilotto, S., Heise, C., Verpelli, C., Tedeschi, G., Maffioli, E., Sala, C., et al. (2014). Phosphorylation of neuronal lysine-specific demethylase 1LSD1/KDM1A impairs transcriptional repression by regulating interaction with CoREST and histone deacetylases HDAC1/2. J. Neurochem. *128*, 603–616.

Trapnell, C., Pachter, L., and Salzberg, S.L. (2009). TopHat: discovering splice junctions with RNA-seq. Bioinformatics *25*, 1105–1111.

Tsang, B., Arsenault, J., Vernon, R.M., Lin, H., Sonenberg, N., Wang, L.-Y., Bah, A., and Forman-Kay, J.D. (2019). Phosphoregulated FMRP phase separation models activity-dependent translation through bidirectional control of mRNA granule formation. Proc. Natl. Acad. Sci. USA *116*, 4218–4227.

Tsien, J.Z., Huerta, P.T., and Tonegawa, S. (1996). The essential role of hippocampal CA1 NMDA receptor-dependent synaptic plasticity in spatial memory. Cell *87*, 1327–1338.

Tyagarajan, S.K., and Fritschy, J.-M. (2014). Gephyrin: a master regulator of neuronal function? Nat. Rev. Neurosci. *15*, 141–156.

Ule, J., and Blencowe, B.J. (2019). Alternative splicing regulatory networks: functions, mechanisms, and evolution. Mol. Cell *76*, 329–345.

Ustianenko, D., Weyn-Vanhentenryck, S.M., and Zhang, C. (2017). Microexons: discovery, regulation, and function. Wiley Interdiscip. Rev. RNA *8*, e1418.

Van Nostrand, E.L., Pratt, G.A., Shishkin, A.A., Gelboin-Burkhart, C., Fang, M.Y., Sundararaman, B., Blue, S.M., Nguyen, T.B., Surka, C., Elkins, K., et al. (2016). Robust transcriptome-wide discovery of RNA-binding protein binding sites with enhanced CLIP (eCLIP). Nat. Methods *13*, 508–514.

Vernon, R.M., and Forman-Kay, J.D. (2019). First-generation predictors of biological protein phase separation. Curr. Opin. Struct. Biol. *58*, 88–96.

Vernon, R.M., Chong, P.A., Tsang, B., Kim, T.H., Bah, A., Farber, P., Lin, H., and Forman-Kay, J.D. (2018). Pi-Pi contacts are an overlooked protein feature relevant to phase separation. eLife *7*, e31486.

Volianskis, A., France, G., Jensen, M.S., Bortolotto, Z.A., Jane, D.E., and Collingridge, G.L. (2015). Long-term potentiation and the role of N-methyl-D-aspartate receptors. Brain Res. *1621*, 5–16.

Vuong, C.K., Black, D.L., and Zheng, S. (2016). The neurogenetics of alternative splicing. Nat. Rev. Neurosci. *17*, 265–281.

Wang, J., Telese, F., Tan, Y., Li, W., Jin, C., He, X., Basnet, H., Ma, Q., Merkurjev, D., Zhu, X., et al. (2015). LSD1n is an H4K20 demethylase regulating memory formation via transcriptional elongation control. Nat. Neurosci. *18*, 1256–1264.

Weyn-Vanhentenryck, S.M., Mele, A., Yan, Q., Sun, S., Farny, N., Zhang, Z., Xue, C., Herre, M., Silver, P.A., Zhang, M.Q., et al. (2014). HITS-CLIP and integrative modeling define the Rbfox splicing-regulatory network linked to brain development and autism. Cell Rep. *6*, 1139–1152.

Wilbertz, J.H., Voigt, F., Horvathova, I., Roth, G., Zhan, Y., and Chao, J.A. (2019). Single-molecule imaging of mRNA localization and regulation during the integrated stress response. Mol. Cell *73*, 946–958.e7.

Wiśniewski, J.R., Zougman, A., Nagaraj, N., and Mann, M. (2009). Universal sample preparation method for proteome analysis. Nat. Methods *6*, 359–362.

Youn, J.-Y., Dunham, W.H., Hong, S.J., Knight, J.D.R., Bashkurov, M., Chen, G.I., Bagci, H., Rathod, B., MacLeod, G., Eng, S.W.M., et al. (2018). High-density proximity mapping reveals the subcellular organization of mRNA-associated granules and bodies. Mol. Cell *69*, 517–532.e11.

Zhong, Y., Karaletsos, T., Drewe, P., Sreedharan, V.T., Kuo, D., Singh, K., Wendel, H.-G., and Rätsch, G. (2017). RiboDiff: detecting changes of mRNA translation efficiency from ribosome footprints. Bioinformatics *33*, 139–141.

Zhou, J., and Parada, L.F. (2012). PTEN signaling in autism spectrum disorders. Curr. Opin. Neurobiol. *22*, 873–879.

Zhu, B., Ramachandran, B., and Gulick, T. (2005). Alternative pre-mRNA splicing governs expression of a conserved acidic transactivation domain in myocyte enhancer factor 2 factors of striated muscle and brain. J. Biol. Chem. *280*, 28749–28760.

STAR★METHODS

KEY RESOURCES TABLE

REAGENT or RESOURCE	SOURCE	IDENTIFIER
Antibodies		
anti-eIF4G1	Cell Signaling	2498; RRID:AB_2096025
anti-eIF4G3	Gift by Nahum Sonenberg	N/A
anti-NMDAR1	Thermo Fisher Scientific	PA3-102; RRID:AB_2112003
anti-GAPDH	Proteintech	10494-1-AP; RRID:AB_2263076
anti-Gephyrin	Synaptic Systems	147 111; RRID:AB_887719
anti-Neuroligin-2	Synaptic Systems	129 203
anti-FMRP	Cell Signaling	4317; RRID:AB_1903978
anti-FXR1	Santa Cruz Biotechnology	sc-374148; RRID:AB_10918113
anti-STAU2	Thermo Fisher Scientific	PA5-78473; RRID:AB_2736660
anti-eIF4E	Cell Signaling	9742; RRID:AB_823488
anti-LARP1	Abcam	ab86359; RRID:AB_1925169
anti-Ataxin-2	Proteintech	21776-1-AP; RRID:AB_10858483
anti-Flag M2	Sigma-Aldrich	F3165; RRID:AB_262044
anti-Puromycin 12D10	MD-Millipore	MABE343; RRID:AB_2566826
anti-RFP	Chromotek	[5F8]; RRID:AB_2336064
anti-Actin	Abcam	ab3280; RRID:AB_303668
anti-TUJ1	Covance	MRB-435P; RRID:AB_663339
anti-MAP2	Abcam	ab5392; RRID:AB_2138153
Bacterial Strains		
BL21-CodonPlus (DE3) Competent Cells	Agilent	230280
Subcloning Efficiency DH5α Competent Cells	Thermo Fisher Scientific	18265017
Chemicals, Peptides, and Recombinant Proteins		
Actinomycin D	Thermo Fisher Scientific	11805017
Kainic acid	Tocris	0222
Domoic acid	Tocris	0269
(S)-3,5-DHPG	Abcam	ab144484
Bicuculline methiodide	HelloBio	HB0893
Picrotoxin	HelloBio	HB0506
CGP 55845	HelloBio	HB0960
Bicuculline	Sigma-Aldrich	14340
6-cyano-7nitroquinoxaline-2,3-dione (CNQX)	Tocris	0190
DL-2-amino-5-phosphonovaleric acid (AP-5)	Tocris	0105
Tetrodotoxin (TTX)	Affix scientific	AF3015
Homoharringtonine	Sigma-Aldrich	SML1091
Puromycin	Sigma-Aldrich	P8833
Emetine	Sigma-Aldrich	E2375
Cycloheximide	Sigma-Aldrich	01810
Cas9 mRNA	Thermo Fisher Scientific	A29378
Casein Kinase II	New England Biolabs	P6010
Opti-MEM I Reduced Serum Medium	GIBCO	31985070
Neurobasal-A medium	Thermo Fisher Scientific	10888-022
GlutaMAX Supplement	Thermo Fisher Scientific	35050-061
N2 Supplement	Thermo Fisher Scientific	17502001
B27 Supplement	Thermo Fisher Scientific	A3653401

(*Continued on next page*)

Continued

REAGENT or RESOURCE	SOURCE	IDENTIFIER
CultureOne Supplement	Thermo Fisher Scientific	A3320201
Laminin	Sigma-Aldrich	L2020
Poly-D-Lysine	Sigma-Aldrich	6407
Poly-L-Lysine	Thermo Fisher Scientific	P8920
KO serum replacement	Thermo Fisher Scientific	10828010
DMEM (high glucose)	Sigma-Aldrich	D5796
FBS	GIBCO	12483-020
FBS premium	MULTICELL	920040
Sodium pyruvate	GIBCO	11360-070
MEM NEAA	GIBCO	11140-050
RNAiMAX	Thermo Fisher Scientific	13778150
X-tremeGENE HP DNA Transfection Reagent	Roche	06366236001
Lipofectamine 2000	Thermo Fisher Scientific	11668019
Dynabeads protein G	Thermo Fisher Scientific	10004D
Turbo DNase	Thermo Fisher Scientific	AM2238
RNase I	Thermo Fisher Scientific	AM2295
Benzonase Nuclease	Sigma-Aldrich	E826
His-SUMO-eIF4G1+MIC (aa 1-200)	This study	N/A
His-SUMO-eIF4G1ΔMIC (aa 1-193)	This study	N/A
His-SUMO-FMRP (aa 445-632)	(Tsang et al., 2019)	N/A
5′6-FAM-sc1 RNA	(Tsang et al., 2019)	N/A
Critical Commercial Assays		
OneStep RT-PCR Kit	QIAGEN	210210
SensiFAST SYBR® No-ROX Kit	BIOLINE	BIO-98005
Maxima First Strand cDNA Synthesis Kit for RT-qPCR	Thermo Fisher Scientific	K1671
SuperScriptIII	Thermo Fisher Scientific	18080044
Syn-PER Synaptic Protein Extraction Reagent	Thermo Fisher Scientific	87793
RNeasy Mini Kit	QIAGEN	74106
Deposited Data		
CLIP-Seq	This study	GEO: GSE141594
CLIP-Seq	(Weyn-Vanhentenryck et al., 2014; Gonatopoulos-Pournatzis et al., 2018)	GEO: GSE112598 and SRP039559
RNA-Seq	This study	GEO: GSE141599
Ribosome profiling	This study	GEO: GSE141599
iTRAQ proteomics	This study	http://massive.ucsd.edu MSV000084658
Proximity ligation proteomics (BioID) data	This study	http://massive.ucsd.edu MSV000083349 and ProteomeXchange: PXD012421
Experimental Models: Cell Lines		
Mouse: CGR8	ECACC	07032901
Mouse: N2A	ATCC	CCL-131
Experimental Models: Organisms/Strains		
C57BL/6J *Eif4g1* microexon deficient mice (*Eif4g1*$^{\Delta MIC/\Delta MIC}$)	This study	N/A
C57BL/6J *Eif4g3* microexon deficient mice (*Eif4g3*$^{\Delta MIC/\Delta MIC}$)	This study	N/A
C57BL/6J *Eif4g1/3* microexon deficient mice (*Eif4g1*$^{\Delta MIC/\Delta MIC}$ & *Eif4g3*$^{\Delta MIC/\Delta MIC}$)	This study	N/A

(*Continued on next page*)

Continued

REAGENT or RESOURCE	SOURCE	IDENTIFIER
Oligonucleotides		
See STAR Methods	This study	N/A
Software and Algorithms		
vast-tools 1.0	(Tapial et al., 2017)	https://github.com/vastgroup/vast-tools
DESeq	(Anders and Huber, 2010)	https://bioconductor.org/packages/release/bioc/html/DESeq.html
Prism 8	Graph.Pad Prism	https://www.graphpad.com/scientific-software/prism/
MS data storage and analysis: ProHits-LIMS	(Liu et al., 2016)	http://prohitsms.com/Prohits_download/list.php
MS Data Significance Analysis of INTeractome analysis: SAINT	(Teo et al., 2014)	Version exp3.3
PausePred	(Kumari et al., 2018)	https://pausepred.ucc.ie/
RiboDiff	(Zhong et al., 2017)	http://public.bmi.inf.ethz.ch/user/zhongy/RiboDiff/
ImageJ	NIH	https://imagej.nih.gov/ij/
Volocity	Quorum Technologies	http://quorumtechnologies.com/index.php/component/content/category/31-volocity-software
Clampfit 10.7	Molecular Devices	N/A
Activity Monitor software	Med Associates Inc.	SOF-812
Ethovision XT software	Noldus	N/A
Video Freeze software	Med Associates Inc.	SOF-843
Trimmomatic	(Bolger et al., 2014)	http://www.usadellab.org/cms/index.php?page=trimmomatic
Tophat	(Trapnell et al., 2009)	http://ccb.jhu.edu/software/tophat/index.shtml
Proteome Discoverer 2.1.0.81 software	Thermo Scientific	N/A
g:Profiler	(Reimand et al., 2016)	https://biit.cs.ut.ee/gprofiler
Cytoscape – Enrichment map	(Isserlin et al., 2014)	http://baderlab.org/Software/EnrichmentMap
RiboSeqR	RiboSeqR	https://bioconductor.org/packages/release/bioc/html/riboSeqR.html
CentriMO	(Bailey and Machanick, 2012)	http://meme-suite.org/doc/centrimo.html
PLAAC	(Lancaster et al., 2014)	http://plaac.wi.mit.edu/
DISOPRED3	(Jones and Cozzetto, 2015)	http://bioinf.cs.ucl.ac.uk/psipred/

LEAD CONTACT AND MATERIALS AVAILABILITY

Further information and requests for resources, reagents and materials should be directed to and will be fulfilled by the Lead Contact, Benjamin J. Blencowe (b.blencowe@utoronto.ca). All unique/stable reagents generated in this study are available from the Lead Contact with a completed Materials Transfer Agreement.

EXPERIMENTAL MODEL AND SUBJECT DETAILS

Cell culture

Mouse neuroblastoma Neuro-2A (N2A) and human SH-SY5Y cells were grown in DMEM (high glucose; Sigma-Aldrich) supplemented with 10% FBS, sodium pyruvate, nonessential amino acids, and penicillin/streptomycin. Mouse embryonic stem cells (mESC) were grown in gelatin coated plates in GMEM supplemented with 100 μM β-mercaptoethanol, 0.1 mM nonessential amino acids, 2 mM sodium pyruvate, 2.0 mM L-glutamine, 5,000 units/mL penicillin/streptomycin, 1000 units/mL recombinant mouse LIF (all Thermo Fisher Scientific) and 15% ES fetal calf serum (ATCC). Cells were maintained at sub-confluent conditions. mESC-derived neurons were generated and cultured as described below. All cell lines were maintained at 37°C with 5% CO_2. Cells were regularly monitored for absence of mycoplasma infection.

In vitro neuronal differentiation

In vitro differentiation of mESCs into glutamatergic neurons was performed as described previously (Gueroussov et al., 2015; Hubbard et al., 2013). The CGR8 mESC lines were maintained for at least 2 passages prior to differentiation and were differentiated into

neurons between 5–35 passages. Initially, 5x10^6 cells were transferred to a 15 cm non-adhesive plate (not coated) containing 30 mL of differentiation medium (GMEM containing 5% KnockOut Serum replacement (Thermo Fisher Scientific), 0.1 mM nonessential amino acids, 1 mM sodium pyruvate, 2 mM L-glutamine, 5,000 units/mL penicillin/streptomycin and without LIF). This point was designated as days *in vitro* (DIV) −8. Half media changes were conducted every 48 hours by collecting cell aggregates to the center of the plates by swirling. The media was supplemented with 6 μM retinoic acid (Sigma-Aldrich) at DIV −4 and DIV −2. On DIV 0, cellular aggregates were dissociated with TrypLE Express for 5 minutes at 37°C. Trypsinization was halted with soybean trypsin inhibitor (Thermo Fisher Scientific) and after gentle dissociation by trituration, cells were pelleted for 5 minutes at 300 x g. Neural progenitors were washed in N2 medium (Neurobasal-A medium with 1x N2 vitamins, 2 mM glutamine and antibiotics (Thermo Fisher Scientific)), counted using a hemocytometer and plated at 1.5 × 10^5 cells/cm^2 in poly-D-Lysine/Laminin coated dishes. The plated neural progenitors were washed with N2 medium after 24 hours to remove residual serum and non-adherent cells. At DIV 2, N2 was replaced with B27 medium (Neurobasal-A supplemented with antibiotics, 2 mM glutamine and 1 x B27 vitamins (Thermo Fisher Scientific)). Subsequently, differentiating neurons underwent full medium changes with B27 on DIV 4, 7 and 10.

Primary neuronal culture

Hippocampi of postnatal day 0 (P0) mice were dissected and dissociated using papain (Worthington) solution. Culturing surfaces were first coated with poly-L-Lysine solution in borax buffer and subsequently coated with Laminin solution in PBS. Hippocampal neurons were cultured in Neurobasal plus media system supplemented with CultureOne supplement, N2 supplement, Glutamax and Penicillin/Streptomycin (GIBCO) and half media changes were performed every 3 days until processing.

In vivo mouse studies

All mouse studies were conducted using male C57BL/6J mice. All experiments were conducted in compliance with the Animals for Research Act of Ontario and the Guidelines of the Canadian Council on Animal Care (CCAC). The Centre for Phenogenomics (TCP) Animal Care Committee reviewed and approved all procedures conducted on animals.

Housing and husbandry conditions for experimental animals

Animal room light cycles were scheduled on at 7 AM and off at 7 PM. Animal holding rooms are supplied with 100% fresh air. Supply and exhaust ventilation exchange rates were set at 10-15 air changes per hour. Room temperature was maintained at 20-22°C and the environmental conditions in the animal facility were monitored by a Siemens Building Automation System. All animals were appropriately housed in compliance with the CCAC Guidelines and the Ontario Ministry of Agriculture, Food and Rural Affairs (OMAFRA) Animals for Research Act. Animal care attendants performed daily husbandry and health checks on all animals. Weaning was performed at 21 days.

METHOD DETAILS

siRNA and plasmid transfections

N2A cells were transfected with 20 nM of siGENOME siRNA pools (Dharmacon) using RNAiMax (Thermo Fisher Scientific) as recommended by the manufacturer. A non-targeting siRNA pool (D-001206-13) was used as control. Cells were harvested 48 hours post transfection.

SH-SY5Y (ATCC CRL-2266) cells were plated on 6-well plates coated with Poly-L-Lysine (0.1% w/v) and transfected on the next day using X-tremeGENE HP DNA Transfection Reagent protocol version 8 (Roche Diagnostics) using a 3:1 DNA to transfection reagent ratio according to the manufacturer's instructions.

Polysome profiling

Mouse brains were dissected in HBSS supplemented with 0.1 μg/ml cycloheximide on ice and immediately frozen on dry ice. Flash frozen cortices (10-15 mg) were homogenized in 500-750 μl polysome lysis buffer (100 mM KCl, 5 mM MgCl2, 10 mM Tris-HCl, pH9, 1% Triton X-100, 1% sodium deoxycholate). Extracts were clarified by centrifugation at 2,500 g for 15 minutes at 4°C and cycloheximide and heparin were added to 0.1 μg/ml and 1 μg/ml, respectively. Cytoplasmic lysates with equal RNA content for control and mutant extracts were adjusted to 500 μl with polysome lysis buffer and then loaded onto 13 mL of a 20%–50% sucrose gradient solution in a polyallomer ultracentrifuge tube. Following centrifugation at 151,000 g at 4°C for 2 hours in a SW41Ti (Beckman) rotor. The fractions were monitored by UV absorbance at 254 nm by ISCO UA-6 UV detector (Teledyne Isco).

RNA extraction and RT-PCR assays

RNA was extracted from cells using the QIAGEN RNeasy Mini Kit as recommended by the manufacturer. To assess Eif4g1 and Eif4g3 microexon splicing, forward and reverse primers were designed to anneal to the constitutively included exons upstream and downstream of each alternative exon, respectively. The primer sequences are provided below:

Hs eIF4G1 F: 5′- TCAGTACGCCACAAGCGAC −3′
Hs eIF4G1 R: 5′- AGCAGGGTAGACATGGGCAG −3′

Hs eIF4G3 F: 5′- CAACCTCAAACCCGTTCTCC −3′
Hs eIF4G3 R: 5′- TGGTAGCTCTAGGAGGCTG −3′
Mm Eif4g1 F: 5′- GGTGTTTAGCACGCCTCAAGC −3′
Mm Eif4g1 R: 5′- TGGGAGGCTGAGTAGGAGATC −3′
Mm Eif4g3 F: 5′- CCAGCCACATTGGTCTATCCTC −3′
Mm Eif4g3 R: 5′- CTGTTTGGGATGGCAGCTCG −3′
Mm Cpeb4 F: 5′- CGTCTAAACTATTCATACCCAGG −3′
Mm Cpeb4 R: 5′- CCATCGGAAACAATGAAGACTGAC −3′
Mm Rps24 F: 5′- AGGCCAATGTTGGTGCTG −3′
Mm Rps24 R: 5′- GCAGCACCTTTACTCCTTCG −3′
Mm Grin1 F: 5′- CTGTCTCCTACACAGCTGGC −3′
Mm Grin1 R: 5′- TTCTCTGCCTTGGACTCACG −3′
Mm Gphn F: 5′- CAAATCCGTGTCGGAGTCCT −3′
Mm Gphn R: 5′- TTTGTGGCCTCTGGAGTGAC −3′
Mm Nlgn2 F: 5′- GTGGTTCACCGACAACTTGG −3′
Mm Nlgn2 R: 5′- CGGATATCTGTGTCTGGCGGA −3′

RT-PCR assays were performed using the OneStep RT-PCR kit (QIAGEN) according to the manufacturer's recommendations, except for RNA from Zebrafish tissues, which was first reverse transcribed into cDNA using oligodT priming with SuperScriptIII (Invitrogen). Reaction products were separated on 3.5% agarose gels. All amplification products shown in agarose gels correspond to expected sizes based on separation of size markers (GeneRuler 1 kb Plus DNA Ladder, Thermo Fisher Scientific). The Percent Spliced In (PSI) values were calculated using the ImageJ software. The intensity of the exon-included band was divided by the sum of the exon-included and exon-skipped bands. The result was multiplied by 100% to obtain the PSI value, which was rounded to the nearest whole integer.

Quantitative RT-PCR

Quantitative RT-PCR (qRT-PCR), was performed after generating first-strand cDNAs from 0.25-3 μg of total RNA using the Maxima H Minus First Strand cDNA synthesis Kit (Thermo Fisher Scientific), as per the manufacturer's recommendations. The cDNA was diluted to 2 ng/μL. qPCR reactions were performed in a volume of 10 μL using 1 μL of diluted cDNA, 500 nM primers and 5 μL SensiFAST SYBR No-ROX Kit (BIOLINE), using a CFX96 Real-Time PCR Detection System (BIO-RAD) as per manufacturer's recommendations. The primers used are provided below.

Mm JunB F: 5′- GCACTGGGGACTTTGAGGGT −3′
Mm JunB R: 5′- TTTCTCTCCCTCCGTGGTGC −3′
Mm Nr4a1 F: 5′- CACAGGGAGTGGGAGCCG −3′
Mm Nr4a1 R: 5′- GAACTCAAGGGCCAGGGGAT −3′
Mm Dusp5 F: 5′- GTGGAAAGCCCGTTCTCAGC −3′
Mm Dusp5 R: 5′- TGGATGCGTGGTAGGCACTT −3′
Mm Arc F: 5′- GCCACACTCGCTAAGCTCCT −3′
Mm Arc R: 5′- CGGCTCCGAACAGGCTAAGA −3′
Mm Fosl2 F: 5′- CCGGGAACTTTGACACCTCG −3′
Mm Fosl2 R: 5′- CCGAGCCAGGCATATCTACCC −3′
Mm cFos F: 5′ - GGGCTCTCCTGTCAACACAC −3′
Mm cFos R: 5′ - CTGGTGGAGATGGCTGTCAC −3′

Ribopuromycylation

Labeling of stalled ribosomes was performed as described previously (Graber et al., 2013, 2017). Briefly, DIV 11 WT and DKO mouse hippocampal neurons were incubated in Neurobasal plus medium supplemented with 5 μM Homoharringtonine for 10 minutes to inhibit translation initiation. To tag stalled ribosomes, the medium was subsequently replaced by Neurobasal plus supplemented with 5 μM Homoharringtonine, 100 μM Puromycin and 200 μM Emetine (Sigma-Aldrich) for 5 minutes. Subsequently, cells were placed on ice and washed with HBSS solution supplemented with 0.0003% digitonin for 2 minutes. Neurons were washed with cold HBSS twice to remove Digitonin. Neurons were then fixed for 15 minutes in 4% paraformaldehyde and 10% sucrose in PBS.

Fluorescence microscopy

CGR8-derived neural precursors were plated on coverslips (coated with poly-D-Lysine/Laminin) in 6 well plates at 1×10^6 cells/well. At DIV 8, cells were fixed in 4% paraformaldehyde/PBS. Fixed cells were permeabilized with 0.1% Triton X-100 in PBS for 10 minutes at room temperature and incubated in blocking solution (5% BSA, 1% normal goat serum and 0.2% Tween 20) for 90 minutes at room

temperature. Staining was performed with primary antibodies diluted in blocking solution for 90 minutes at 37°C (antibody dilutions: rabbit anti-TUJ1, Covance MRB-435P at 1:2,000; chicken anti-MAP2, Abcam ab5392 at 1:10,000; anti-Puromycin 12D10, MD-Millipore MABE343 at 1:1,000). Coverslips were washed three times with PBS containing 0.2% Tween 20 and incubated with secondary antibodies diluted in blocking buffer (anti-mouse IgG Alexa Fluor 488 at 1:1,000; anti-rabbit IgG Alexa Fluor 594 at 1:1,000) at room temperature for 60 minutes. Cells were washed five times with PBS containing 0.2% Tween 20 prior to mounting with DACO fluorescence fixing medium. DNA was labeled with Hoechst 33258 (Sigma-Aldrich) to indicate nuclei.

SH-SY5Y cells, 16-18 hours post-transfection, were fixed with 4% formaldehyde and mounted using Vectashield mounting media containing 4′ ,6-Diamidino-2-phenylindole dihydrochloride (DAPI) (Vector Laboratories). Images were acquired using 20x (to view fields of cells) and 60x oil immersion objective lenses (Nikon D-eclipse C1 confocal system).

Co-immunoprecipitation experiments

Flag-tagged EIF4G1 ± microexon constructs were transiently transfected into N2A cells grown on 10cm plates using Lipofectamine 2000. After 48 hours, cells were washed in cold phosphate buffered saline (PBS) and lysed in 1 mL of lysis buffer (50 mM HEPES–KOH pH 8.0, 100 mM KCl, 2 mM EDTA, 0.1% NP40, 10% glycerol and supplemented with protease and phosphatase inhibitors). Lysates were subject to sonication (15 × 1 s pulses with 1 s in between at 30% power). For nuclease digestion, 10 μg RNase A, 25 Units RNase T1 and 75 Units of benzonase were added and lysates were incubated at 37°C with shaking for 10 minutes. Lysates were cleared in a microcentrifuge by spinning at 15,000 g for 20 minutes at 4°C. Anti-flag immunoprecipitation was performed using magnetic Dynabeads protein G (Thermo Fisher Scientific) complexed with anti-Flag M2 antibody (Sigma-Aldrich). Antibody was incubated with lysates for 1 hours at 4°C followed by incubation with washed Dynabeads protein G for 3 hours at 4°C with rotation. Following incubation, complexes were washed 5 times with lysis buffer. Elution was performed in 1x Laemmli buffer at 95°C for 5 minutes.

Puromycin labeling

CGR8-derived neurons from two independent WT and DKO clones (DIV 8) were treated with puromycin (0.1 μg/ml final) for 15 minutes, 30 minutes and 60 minutes. Cells were rinsed with PBS then extracted with lysis buffer supplemented with protease and phosphatase inhibitors. Immunoblots were prepared and developed as described below. Puromycin incorporation was assessed by measuring the immunoblot intensity of all protein bands after subtracting background.

Preparation of synaptoneurosomal fractions

Synaptoneurosomes were isolated using Syn-PER Synaptic Protein Extraction Reagent (Thermo Fisher Scientific) following the manufacturer's recommendation. Briefly, dissected hippocampal tissues from WT and *Eif4g1*$^{\Delta MIC/\Delta MIC}$ mice were weighed and resuspended in 5x times volume of Syn-PER Reagent (500 μl per 100 mg brain tissue) supplemented with protease and phosphatase inhibitors. Dounce homogenization with 10 strokes was followed by centrifugation at 1,200 g for 10 minutes at 4°C. The supernatant was transferred to a fresh tube and centrifuged at 14,000 g for 10 minutes at 4°C. The supernatant was removed and the pellet resuspended in Syn-PER Reagent containing 1x Laemmli buffer (100 μl for 100 mg of original brain tissue).

Immunoblotting

Cell lysates were mixed with Laemmli buffer and heated at 95°C for 5 min, separated on variable percentage SDS-PAGE gels, and transferred to PVDF membrane. Blots were incubated for one hour at room temperature with the following primary antibodies at the specified dilutions in 5% milk:

- Rabbit anti-eIF4G1 (Cell Signaling; #2898) at 1:1,000
- Rabbit anti-eIF4G3 (Sonenberg lab) at 1:2,000
- Rabbit anti-NMDAR1 (Thermo Fisher Scientific; PA3-102) at 1:500
- Rabbit anti-Gapdh (Proteintech; 10494-1-AP) at 1:2,000
- Rabbit anti-Gephyrin (Synaptic Systems; 147 111) at 1:2,000
- Rabbit anti-Neuroligin-2 (Synaptic Systems; 129 203) at 1:1,000
- Rabbit anti-FMRP (Cell signaling; #4317) at 1:1,000
- Mouse anti-FXR1 (Santa Cruz Biotechnology; B-2; sc-374148) at 1:500
- Rabbit anti-STAU2 (Thermo Fisher Scientific; PA5-78473) at 1:500
- Rabbit anti-eIF4E (Cell signaling; #9742) at 1:1,000
- Rabbit anti-LARP1 (Abcam; ab86359) at 1:2,000
- Rabbit anti-Ataxin-2 (Proteintech; 21776-1-AP) at 1:2,000
- Mouse anti-Flag M2 (Sigma-Aldrich; F3165) at 1:2,000
- Mouse anti-Puromycin 12D10 (MD-Millipore; MABE343) at 1:1,000
- Rat anti-RFP (Chromotek; [5F8]) at 1:500
- Mouse anti-Actin (Abcam; ab3280) at 1:5,000

Individual-nucleotide Resolution Cross-linking and Immunoprecipitation (iCLIP-Seq)

iCLIP was performed as described previously (Huppertz et al., 2014). Srrm4, Srrm3 or GFP (as a negative control) were immunoprecipitated from CGR8 mESC-derived neurons induced for 36 hours with 2 μg/ml doxycycline to express Flag-tagged Srrm4, Srrm3 or GFP, respectively. Initially, we generated CGR8 mESC single cell clones expressing Flag-tagged Srrm4 or GFP using the PiggyBac transposase system. mESC clones were differentiated into cortical glutamatergic neurons as described above. Neurons (DIV 10) were crosslinked (0.20 J/cm^2) at 254 nm with a Stratalinker 1800. Three independent replicates were used for generating iCLIP libraries. Lysates were treated with Turbo DNase (Thermo Fisher Scientific) and RNase I (Thermo Fisher Scientific) diluted in PBS 500 times for 5 minutes at 37°C to digest genomic DNA and trim RNA to short fragments of an optimal size range. RNA-protein complexes were purified using 100 μL of protein G Dynabeads (Thermo Fisher Scientific) and 10 μg of anti-Flag (Sigma-Aldrich) antibody. Following stringent high salt washes, the immunoprecipitated RNA was 3′ end dephosphorylated and ligated to a pre-adenylated adaptor at the 3′ end as described previously (Van Nostrand et al., 2016). After extensive additional washes and buffer exchange, the immunoprecipitated RNA was 5′ end-labeled using ATP [γ-^{32}P]. The purified protein-RNA complexes were separated with SDS-PAGE and transferred to a nitrocellulose membrane (Protran). Protein was digested using proteinase K, the RNA was purified (using phenol/chloroform) and reverse transcribed into cDNA. The cDNA was size selected by resolving samples on a 6% TBE-Urea gel, circularized to add the adaptor to the 5′ end, digested at the internal BamHI site, and then PCR amplified using AccuPrime SuperMix I (Thermo Fisher Scientific). The final PCR libraries were purified by agarose gel electrophoresis using gel extraction columns (QIAGEN). Eluted DNA was mixed at a ratio of 1:5:5 from the low, middle, and high fractions and submitted for sequencing.

For Flag-Srrm4 iCLIP-Seq the barcoded primers used were: Rt1clip, Rt9clip and Rt13Clip. For Flag-Srrm3 iCLIP-Seq the barcoded primers used were: Rt10clip, Rt13clip and Rt14Clip; and for Flag-GFP the barcoded primers used were Rt6clip, Rt14clip and Rt16clip:

Rt1clip: /5Phos/NNAACCNNNAGATCGGAAGAGCGTCGTGgatcCTGAACCGC;
Rt6clip: /5Phos/NNCCGGNNNAGATCGGAAGAGCGTCGTGgatcCTGAACCGC;
Rt9clip: /5Phos/NNGCCANNNAGATCGGAAGAGCGTCGTGgatcCTGAACCGC;
Rt10clip: /5Phos/NNGACCNNNAGATCGGAAGAGCGTCGTGgatcCTGAACCGC;
Rt13clip: /5Phos/NNTCCGNNNAGATCGGAAGAGCGTCGTGgatcCTGAACCGC;
Rt14clip: /5Phos/NNTGCCNNNAGATCGGAAGAGCGTCGTGgatcCTGAACCGC;
Rt16clip: /5Phos/NNTTAANNNAGATCGGAAGAGCGTCGTGgatcCTGAACCGC.

CRISPR/Cas9-directed deletion of Eif4g microexons in CGR8 cells

CGR8 mESC lines deficient of both Eif4g1 and Eifg3 microexons (DKO) were generated as described previously using the CRISPR-Cas9 system (Gueroussov et al., 2015; Ran et al., 2013). Briefly, 20-nt guide sequences were designed to have minimum off-target effects using the online CRISPR design tool provided by the Zhang laboratory (http://tools.genome-engineering.org). Two independent guides targeting sequences upstream (designated as U1: 5′- GTAGTATAGTAGTAAAGAGC −3′ and U2: 5′- CTCTTTACTACTA TACTAGG −3′ guides) and downstream (designated as D1: 5′- CAGATTGGGATGGTCACGGT −3′ and D2: 5′- CACGATCCCTT CAAGTACCG −3′) of *Eif4g1* microexon as well as two independent guides targeting sequences upstream (designated as U1: 5′- GTGCTCGCGTCCCGAGTGGA −3′ and U2: 5′- CTTGGTAACAGACGTACACT −3′ guides) and downstream (designated as D1: 5′- TAGGTACGGCTGCCGCGGGC −3′ and D2: 5′- CGGCAGCCGTACCTAGGCTA −3′) of *Eif4g3* microexon were chosen. The guide sequences were cloned individually into the pSpCas9(BB)-2A-Puro (PX459) vector (Addgene #48139), as described previously (Ran et al., 2013). For the simultaneous deletion of both *Eif4g1* and *Eif4g3* microexons, CGR8 cells were simultaneously transiently transfected with PX459-U1 and PX459-D1 or PX459-U2 and PX459-D2 plasmids using Lipofectamine 2000 (Thermo Fisher Scientific) following the manufacturer's instructions. 24 hours post-transfection, 1 μg/ml Puromycin was applied to the media to select for transfected cells. Five days post-transfection the cells were plated on gelatin-coated 96-well plates at a concentration of 0.5 cells/well in order to achieve clonal mESC lines. Ten days later, the clones were expanded and screened for homozygous deletion of *Eif4g1* and *Eif4g3* microexons. For screening cell clones, gDNA was extracted using the Phusion Human Specimen Direct PCR Kit (Thermo Fisher Scientific) as per the manufacturer's recommendations. Editing was detected by PCR amplification across *Eif4g1* and *Eif4g3* microexons using the following primers:

Eif4g1 forward: 5′- GGACTGTGGCTTGAGTAGGCTT −3′
Eif4g1 reverse: 5′- CGCATGGCGATCAATCCTTCC −3′
Eif4g3 forward: 5′- CAGTGGAGTAGAAGTGCTGACG −3′
Eif4g3 reverse: 5′- CAAGGCAGTCTCCATGCTCAG −3′

Positive clones were analyzed further to confirm microexon deletion for both alleles by using reverse primers that recognize the microexon sequence and by Sanger sequencing.

Quantitative proteomics

Sample preparation

Three biological replicates of WT and double Eif4g1 and Eif4g3 microexon deficient stem cell-derived neuros (DIV 3 and DIV 8) were dissolved in 2 mL 4% SDS with 4 μL of 500 × stock of protease inhibitor cocktail (Cat #P8340, Sigma-Aldrich). The samples were sonicated at 4°C using three 10 s bursts with 10 s pauses at 35% amplitude and then centrifuged at 20,000 g at 4°C for 50 minutes. Protein concentration was determined by a BCA assay (Cat #500-0119, Bio-Rad). The supernatants were stored at – 80°C.

A filter-aided sample preparation (FASP) method was used for protein digestion (Wiśniewski et al., 2009). 100 μg of protein from each sample was dissolved in 200 μL of a solution containing 4% SDS in 50 mM ammonium bicarbonate (pH 8). Then, 100 mM DTT (dissolved in 50mM ammonium bicarbonate) was added to the sample and the mixture was heated at 90°C for 10 minutes for protein denaturation and reduction. The mixture was added to a 10 kDa centrifugal filter unit (Cat #VN01H02, Sartorius), followed by centrifugation at 14,000 g for 15 minutes. Alkylation was achieved by addition of 200 μL of a 20 mM iodoacetamide (IAA) solution in 50 mM ammonium bicarbonate directly on the membrane. The mixture was kept at room temperature for 20 minutes (in dark) and then centrifuged at 14,000 g for 15 minutes. The proteins on the membrane were sequentially washed 5 times with 150 μL of 8 M urea (dissolved in 100 mM TEAB), followed by three washes with 150 μL of 100 mM TEAB to remove urea. Finally, 150 μL of 100 mM TEAB was loaded on each filter and 4 μL of 1 μg/μL of trypsin solution (Cat #V5111, Promega) was added to each unit. The filter units were gently vortexed for 5 minutes to mix the trypsin and proteins, then transferred to a 37°C water bath for 12 hours for tryptic digestion. After digestion, the units were centrifuged at 15,000 g for 15 minutes, and the flow-through containing the peptides was collected. To increase peptide recovery from the membrane, the membrane was further washed with 100 mM TEAB and the flow-through from those two steps was then combined.

iTRAQ labeling and high pH fractionation

The peptides from each sample were labeled with iTRAQ 8 plex reagents (Cat #4390812, Sciex) according to the manufacturer's instructions as follows: WT day 3, iTRAQ reagent 113; WT day 8, iTRAQ reagent 114; DKO day 3, iTRAQ reagent 116; DKO day 8, iTRAQ reagent 117. Differentially labeled peptides were mixed and then fractionated using the Pierce TM High pH Reversed-Phase Peptide Fractionation Kit (Cat #84868). Eight fractions were collected using: 10, 12.5, 15, 17.5, 20, 22.5, 25 and 50% acetonitrile. Those fractions were subsequently vacuum-centrifuged to dryness, resuspended in 10 μL of 5% formic acid and half of it was analyzed by LC-MS/MS.

Liquid Chromatography and Mass Spectrometry

LC-MS/MS was performed using an Eksigent 425 nano Ultra HPLC system and a Thermo Fisher Scientific Orbitrap Fusion Lumos mass spectrometer. Samples were loaded using an autosampler directly onto a home-made 75 μm ID × 15 cm packed tip column filled with C 18 particles (3 μm, Reprosil). Digested peptides were separated with a 112 minutes linear gradient from 4% solvent B (0.1% formic acid in acetonitrile) to 30% solvent B (0.1% formic acid in acetonitrile), at a flow rate of 200 nL/min. The run time was 180 minutes for each fraction, including sample loading and column reconditioning. Data-dependent acquisition was performed using the Xcalibur 4.0 software in positive ion mode at a spray voltage of 2.5 kV. Survey spectra were acquired in the Orbitrap with a resolution of 120,000 and a mass range from 350 to 1500 m/z. For HCD scans, the collision energy was set at 35, maximum inject time was 54 ms and the AGC target was 1.0e5. We used an isolation window of 0.7 m/z. Ions selected for MS/MS were dynamically excluded for 20 s after fragmentation.

RNA sequencing

RNA was extracted from two sets of WT and CRISPR edited DKO CGR8-derived neurons (DIV 8) and rRNA-depleted libraries were generated using the TruSeq Illumina library preparation kit (Epicenter) following manufacturer's recommendation. The quantified pool was hybridized at a final concentration of 2.1 pM and sequenced by single-end 51 nucleotides reads on the Illumina HiSeq2500 platform using v4 SBS chemistry and resulting in an average of 48.5M reads per sample.

Ribosome profiling

Two sets of WT and DKO CGR8 clones were differentiated to cortical glutamatergic neurons (DIV 8) as described above. Cells were treated with 100 μg/ml cyclohexamide for 5 minutes. Ribosome profiling was performed using ARTseq Ribosome Profiling Kit (Epicenter) following the manufacturer's recommendation. The quantified pool was hybridized at a final concentration of 2.1 pM and sequenced by single-end 51 nucleotides reads on the Illumina HiSeq2500 platform using v4 SBS chemistry and resulting in an average of 52.25M reads per sample.

Generation of a stable N2A Flp-In rtTA3 cell lines

Generation of cell lines and sample preparation for BioID experiments was performed as previously described (Gonatopoulos-Pournatzis et al., 2018). Briefly, inducible N2A Flp-In rtTA3 stable cell lines expressing either the eIF4G1+MIC or eIF4G1ΔMIC isoforms were generated by co-transfection of 200 ng of a rtTA3 compatible pCDNA5/FRT plasmid (Thermo Fisher Scientific, V6010-20), with 2μg of pOG44 Flp-recombinase expression vector (Thermo Fisher Scientific, V600520). Cell lines with successful cDNA integration were selected and maintained using 200 μg/mL Hygromycin. Transgene expression was induced by addition of 2 μg/mL Doxycycline.

For BioID experiments, N2A Flp-In cell lines were grown to ~70% confluency in a 15 cm plate and expression was induced for 24 hours with 2 μg/mL Doxycycline, in the presence of 50 μM biotin. Cell pellets were collected from one 15 cm plate for each sample and stored at −80°C prior to BioID purification.

BioID Sample Preparation for MS

BioID experiments were performed essentially as described in Lambert et al. (2015). For BioID sample preparation, cell pellets for eIF4G1+MIC, eIF4G1ΔMIC, and control samples (BirA*-Flag-GFP, and BirA*-Flag-empty) were lysed using an ice cold RIPA buffer containing 50 mM Tris-HCl (pH 7.5), 150 mM NaCl, 1% Triton X-100, 1 mM EDTA, 1 mM EGTA and 0.1% SDS, with freshly added 0.5% sodium deoxycholate and protease inhibitor cocktail (Sigma-Aldrich P8340, 1:500) at a 1:10 pellet weight to volume ratio. Lysates were sonicated for 30 s using three 10 s bursts (35% amplitude) and incubated for 30 minutes at 4°C with 1 μL of Benzonase Nuclease (Sigma-Aldrich, E8263, 250U). Lysates were then cleared by centrifugation at 20,000 *rcf.* for 20 minutes at 4°C.

Following centrifugation, equal volumes of eIF4G1+MIC and eIF4G1ΔMIC lysates were transferred to tubes containing 60 μL of streptavidin-Sepharose bead slurry (GE Healthcare, Cat 17-5113-01). The lysate and streptavidin bead mix were incubated for 3 hours at 4°C with rotation to allow capture of biotinylated proteins. After purification, the streptavidin beads were pelleted (6000 rpm, 30 s), and the supernatant removed. For all samples, the streptavidin beads were resuspended in RIPA lysis buffer and transferred to a new microcentrifuge tube. A series of five sequential washes were then performed, once with RIPA lysis buffer, twice with TAP buffer (50 mM HEPES-NaOH (pH 8.0), 100 mM NaCl, 2 mM EDTA, and 10% glycerol), and twice with 50 mM ammonium bicarbonate (ABC) at pH 8 to remove non-biotinylated proteins and residual RIPA lysis buffer. Following the final wash, residual ABC was pipetted off the beads and replaced with 60 μL of ABC containing 1 μg of trypsin (Sigma-Aldrich, T6567). Samples were incubated overnight with rotation at 37°C. The supernatant was then removed to a new tube and the beads rinsed with an additional 60 μL of ABC buffer to collect the digested peptides (total volume of ~120 μL). A second trypsin digest was then performed with 0.5 μg of trypsin for another 4 hours at 37°C after which samples were acidified with formic acid to a final concentration of 2.5% and dried in a centrifugal evaporator.

BioID mass spectrometry data acquisition

BioID samples were analyzed by mass spectrometry in two biological replicates. For each sample, digested peptides were dissolved in 24 μL 5% formic acid with 5 μL of each sample directly loaded into a 15 cm 100 μm ID emitter tip packed in-house with 3.5 μm Reprosil C18. Peptides were eluted from the column over a 90 minutes gradient using a 425 NanoLC (Eksigent, Redwood, CA) and analyzed using a TripleTOF™ 6600 instrument (AB SCIEX, Concord, Ontario, Canada) operated in Data Dependent Acquisition (DDA) mode as previously described (Gonatopoulos-Pournatzis et al., 2018).

Protein phase separation analysis

Recombinant protein expression and purification

cDNA encoding the prion-like domain of eIF4G1 with and without the MIC was digested using BamHI and XhoI restriction enzymes and ligated into the multiple cloning sites of pET-SUMO vector (Thermo Fisher Scientific).

His-SUMO-eIF4G1+MIC (aa 1-200), His-SUMO-eIF4G1ΔMIC (aa 1-193), or His-SUMO-FMRP (aa 445-632) (Tsang et al., 2019) vectors were transformed into *Escherichia coli* BL21 (DE3) codon plus cells (Agilent) and grown at 37°C in LB medium. Protein expression was induced with 0.25 mM Isopropyl β-D-1-thiogalactopyranoside (IPTG) at OD600nm of ~0.6 and grown overnight at 25°C. Cells were pelleted and lysed via sonication in a buffer containing 25 mM Tris pH 8.0, 6 M guanidinium hydrochloride (GdnHCl), 500 mM NaCl, 20 mM imidazole and 2 mM DTT. Cleared lysate was loaded onto a 5 mL HisTrap column (GE Healthcare) equilibrated in lysis buffer. The HisTrap column was extensively washed with 10 column volumes (CVs) of lysis buffer and the GdnHCl was removed by washing the column with 20 CVs of lysis buffer without GdnHCl. The protein was then eluted in 25 mM Tris pH 8.0, 500 mM NaCl, 300 mM imidazole and 2 mM DTT. Fractions containing the protein of interest were confirmed by Coomassie staining of SDS-PAGE gels and pooled together. The His-SUMO tag was cleaved off from the fusion protein using a SUMO protease, ULP, added to the pooled elutions. The cleavage reaction was incubated at room temperature for 3 hours and completion of the ULP reaction was confirmed using Coomassie stained SDS-PAGE gels. The sample was then concentrated with ultrafiltration to ~2 mL, filtered through a 1 μm filter and loaded onto a Superdex 75 HiLoad 16/600 gel filtration column (GE Healthcare) equilibrated with 50 mM Tris pH 8.0, 4 M GdnHCl, 150 mM NaCl and 2 mM DTT. Pure fractions containing the protein of interest were confirmed using Coomassie stained SDS-PAGE and concentrations were determined using a Bradford protein assay. Proteins were stored at −20°C and dialyzed into assay buffers when needed.

In vitro Phosphorylation of FMRP

Recombinant $FMRP^{445-632}$ was phosphorylated *in vitro* as previously described (Tsang et al., 2019). Briefly, purified 100 μM of $FMRP^{445-632}$ (~5-10 mL) was mixed with 5 μL Casein Kinase II (New England Biolabs) in a phosphorylation buffer containing 25 Tris pH 8.0, 100 mM KCl, 10 mM $MgCl_2$, 4 mM ATP, 0.5 mM EGTA and 2 mM DTT. The phosphorylation reaction was dialyzed against 4 L of the same buffer at room temperature and the reaction was quenched with the addition of GdnHCl. The quenched phosphorylation reaction was then concentrated to ~2 mL and passed through a Superdex 75 HiLoad 16/600 gel filtration column (GE Healthcare). On average, 8 to 10 phosphorylation sites were added as determined by mass spectrometry. The phosphorylated protein was dialyzed into assay buffers when needed.

Fluorescence labeling of FMRP recombinant proteins

Fluorescein (FITC) dye was added via a maleimide linkage to a single endogenous cysteine in $FMRP^{445-632}$ or $pFMRP^{445-632}$ (C584). First, purified $FMRP^{445-632}$ or $pFMRP^{445-632}$ was dialyzed into a buffer containing 25 mM Tris pH 7.5, 100 mM NaCl and 4 M GdnHCl. The proteins were passed through a Hi-Trap desalting column (GE-healthcare) to ensure that any residual reducing agents were removed before reacting the proteins with 5X excess FITC dye (Lumioprobe). The labeling reaction was incubated at room temperature for 3 hours and quenched with excess DTT. Unreacted dye was removed by dialysis and then passing the dialyzed protein through a Hi-Trap desalting column (GE-healthcare) equilibrated with 50 mM Tris pH 7.5, 100 mM NaCl, 4 M GdnHCl and 2mM DTT. Dye separation was confirmed by running the labeled samples on SDS-PAGE gel and using a fluorescence reader to detect any remaining free dye.

Fluorescence polarization

The 36-mer RNA oligo sc1 (5′-GCUGCGGUGUGGAAGGAGUGGUCGGGUUGCGCAGCG-3′) was labeled with a 5′ 6-FAM dye (Sigma-Aldrich). Increasing concentrations of eIF4G1+MIC or eIF4G1ΔMIC were titrated into 25 nM of 5′6-FAM-sc1 in buffer containing 25 mM Na_2PO_4 pH 7.4, 2 mM DTT and 0.01% NP-40. The protein-RNA mixture was equilibrated at room temperature for 1 hour and fluorescence polarization was monitored in a black 384-well plate (3820 Corning) with a SpectraMax i3x Multi-Mode Plate reader (Molecular Devices) at 25°C. Averaged values represent three independent biological replicates and dissociation constants (KD) was obtain fitting the data using a Hill plot binding model (Equation 1).

$$Fp = \frac{MaxFP \times [FMRP]^h}{Kd^h + [FMRP]^h} \quad \text{(eq 1)}$$

Turbidity measurements

30 μM of eIF4G1 with or without MIC was mixed with 5 μM sc1 RNA, 60 μM $FMRP^{445-632}$ or 60 μM $pFMRP^{445-632}$ in buffer containing 25 mM Na_2PO_4 pH 7.4 and 2 mM DTT. 20 μL of the mixture was placed in a 384 clear bottom plate (Corning 3544) and incubated at room temperature for 3 minutes before reading the turbidity measurements at 600 nm using a SpectraMax i3x Multi-Mode Plate reader (Molecular Devices) at 25°C. All turbidity measurements were repeated with at least 8 independent replicates for each condition.

Fluorescence microscopy imaging of phase-separated samples

10 μM of FITC-pFMRP/$FMRP^{445-632}$ or 5′6FAM-sc1-RNA was mixed with 80 μM of eIF4G1 with or without the MIC to induce phase separation. All samples were prepared in buffer containing 25 mM Na_2PO_4 pH 7.4 and 2 mM DTT. After mixing, samples were incubated at room temperature for 5 minutes and then half of the mixture was transferred to a 96 glass well plate (Eppendorf). Fluorescence images were acquired on a confocal Leica DMi8 microscope equipped with a Hamamatsu C9100-13 EM-CCD camera and 63x/1.4 (O) objective. FITC fluorescence was detected using a 491 nm (50 mW) laser. All images represent a single focal plane focused on the surface of the slide. Images were processed with Volocity software (Perkin-Elmer) and ImageJ (NIH).

Eif4g1 and *Eif4g3* microexon deletion mouse lines

The *Eif4g1* and *Eif4g3* deletion mutants were generated by direct delivery of Cas9 reagents to C57BL/6J (The Jackson Laboratory, Stock 000664) mouse zygotes at TCP (Toronto, ON, Canada) as described previously (Gertsenstein and Nutter, 2018). Briefly, gRNAs with the desired spacer sequence (STAR Table 1) were synthesized by *in vitro* transcription from a PCR-derived template. A microinjection mix of 20 ng/μL Cas9 mRNA (Thermo Fisher Scientific A29378) and 10 ng/μL each of four gRNAs, two on either side of the target site, for the individual target gene was microinjected into C57BL/6J zygotes. Injected zygotes were incubated in KSOMAA media (Zenith Biotech, ZEKS-50) at 37°C with 6% CO2 until same-day transfer into CD-1 (Charles River Labs, Strain 022) surrogate host mothers.

PCR primers flanking the gRNA target sites (em primers, STAR Table 1) and at least 150 bp from the predicted deletion junction, were used to amplify the region of interest from founder progeny. Founders with the correct PCR amplicon size were selected for breeding with C57BL/6J mice to produce N1 progeny that were confirmed by sequence analysis of PCR amplicons using the same PCR primers for the deletion mutation.

Brain slice preparation and electrophysiological recordings

Acute brain slices were prepared from male $Eif4g1^{\Delta MIC/\Delta MIC}$ mice (C57BL/6J background) and wild-type interleaved controls (P71-105) in accordance with a protocol approved by TCP Animal Care Committee (#20-0292H). The experimenter was blind to genotype during data acquisition and analysis. Isoflurane was administered, and the mouse was observed until a deep state of anesthesia was achieved, indicated by a loss of spinal reflexes. Subsequently, the mouse was decapitated and the brain was immediately submerged in ice-cold, oxygenated, 'dissection' artificial cerebrospinal fluid (aCSF) containing (in mM): 124 NaCl, 3 KCl, 24 $NaHCO_3$, 1.25 NaH_2PO_4, 0 $CaCl_2$, 2 $MgCl_2$ and 10 glucose. The cerebellum was removed with a scalpel, and coronal brain slices (400 μm) containing the dorsal hippocampus were prepared using a vibratome (VT1000S, Leica Biosystems). Slices were allowed to recover at room temperature for at least 2 hours in a submerged incubation chamber containing oxygenated recording aCSF, which was the same as dissection aCSF except for containing 2 mM $CaCl_2$ and 1 mM $MgCl_2$. A slice was transferred to a submerged recording chamber continuously perfused with oxygenated aCSF (2.0 mL/min) at a temperature of 28°C. Synaptic responses were evoked

STAR Table 1. Sequences used for production of *Eif4g1* and *Eif4g3* microexon deletions

Name	Sequence (5′-3′)	Target site
Eif4g1_gRNA_U5	TTACTACTATACTAGGAGGT	Chr16:20674569-20674588 (+1)
Eif4g1_gRNA_U3	AAAGACGACAATTATCCCCA	Chr16:20674745-20674764 (−1)
Eif4g1_gRNA_D5	CACGATCCCTTCAAGTACCG	Chr16:20675015-20675034 (−1)
Eif4g1_gRNA_D3	GATGTTATCTAGCTGTTAGG	Chr16:20675067-20675086 (+1)
Eif4g3_gRNA_U5	CTTGGTAACAGACGTACACT	Chr4:138095619-138095638 (−1)
Eif4g3_gRNA_U3	GTGCTCGCGTCCCGAGTGGA	Chr4:138095727-138095746 (+1)
Eif4g3_gRNA_D5	CGGCAGCCGTACCTAGGCTA	Chr4:138096069-138096088 (−1)
Eif4g3_gRNA_D3	GTCACTGACACTCTAAAGAC	Chr4:138096231-138096250 (+1)
Eif4g1_wt_F1	GACACAAATGAACACGCCTTCTC	Chr4:20674281-20674303 (+1)
Eif4g1_wt_R1	GTGACCATCCCAATCTGTGTCTAG	Chr4:20674874-20674897 (1)
Eif4g1_em_F1	GACACAAATGAACACGCCTTCTC	Chr4:20674281-20674303 (+1)
Eif4g1_em_R1	CTGGGAAGGGATCATCATTACTTGG	Chr4:20675451-20675475 (−1)
Eif4g3_wt_F1	CGCACAAGATGAACAGTTCTGTAG	Chr4:138095392-138095415 (+1)
Eif4g3_wt_R1	CTCCAGAGAAGAATCAGAACTACGC	Chr4:138095764-138095788 (−1)
Eif4g3_em_F1	CGCACAAGATGAACAGTTCTGTAG	Chr4:138095392-138095415 (+1)
Eif4g3_em_R1	GAACTGGCATTTCCCTAAGCACTAC	Chr4:138096459-138096483 (−1)

from the Schaffer collateral pathway using a concentric bipolar platinum/iridium electrode (FHC) and stimulator (Multi Channel Systems, Model STG-4002). Field excitatory postsynaptic potentials (fEPSPs) were recorded with a borosilicate electrode (1.0 – 2.5 MΩ tip resistance) filled with aCSF placed in the stratum radiatum 150-200 μm from the stimulating electrode. Responses were collected using WinLTP software (http://winltp.com; (Anderson and Collingridge, 2007)) with low-pass filtering at 4 kHz using a MultiClamp 700B amplifier (Molecular Devices) and digitized at 20 or 40 kHz with a USB-6341 digitizer (National Instruments). At the beginning of each recording, an input-output curve was generated (stimulus intensities: 5, 10 – 70 μA, Δ = 10 μA). Additionally, a paired-pulse curve was generated by delivering two stimuli at varying paired pulse intervals (400, 200, 100, 50 and 40 ms) at a stimulus intensity of 25 μA; paired-pulses were delivered once every 30 s. After collecting basal synaptic properties, the baseline intensity was set to evoke a slope ~40% of the value at which a population spike was first observed. In all cases responses were evoked once every 30 s. A stable baseline was achieved for 30 minutes before delivering LTP induction stimuli. LTP was induced using 100 Hz stimulation for 1 s (tetanic stimulation), delivered either 1 time or 4 times with 5 minutes spacing in between each tetanus train. For DHPG-LTD experiments, bicuculline methiodide (10 μM; HelloBio), picrotoxin (50 μM; HelloBio) and CGP 55845 (100 nM; HelloBio) were included in the aCSF, as well as 2 mM $MgCl_2$ (instead of 1 mM), to facilitate LTD induction (Palmer et al., 1997). In these experiments, input-output or paired-pulse ratio curve were not performed, and basal responses were set to ~0.75 mV. (S)-3,5-DHPG (100 μM; Abcam) was bath applied for 10 minutes to induce LTD. Data were analyzed using ClampFit 10.7 (Molecular Devices); the slope of the fEPSPs was taken from 20 – 60% of the maximum amplitude of each individual response. Data are presented as the average of 2 responses, normalized to the last 10 minutes of the baseline period.

Spontaneous synaptic transmission recordings

Mice were anesthetized with isoflurane, brains were quickly removed and sliced (300 μm thick coronal plane) with a Vibratome sectioning system in modified aCSF consisting of 180 mM sucrose, 25 mM sodium bicarbonate, 25 mM glucose, 2.5 mM KCl, 1.25 mM sodium phosphate, 2 mM $MgCl_2$, 1 mM $CaCl_2$, 0.4 mM sodium ascorbate, and 3 mM sodium pyruvate, and saturated with 95% O_2/5% CO_2 (pH 7.4, osmolarity: ~305 mOsm). Slices were allowed to recover for at least 1 hour in 35–37°C aCSF consisting of 125 mM NaCl, 25 mM glucose, 25 mM sodium bicarbonate, 2.5 mM KCl, 1.25 mM sodium phosphate, 1 mM $MgCl_2$, and 2 mM $CaCl_2$, and saturated with 95% O_2/5% CO_2 (pH 7.4, osmolarity: ~305 mOsm). Recordings were performed in whole-cell configuration and pipettes were pulled from thin-walled borosilicate glass (TW-150 F, World Precision Instruments) to resistances of 5–7 MΩ with a Sutter Instruments P-87 (Novato). Pipettes were filled with an internal solution containing 130 mM potassium gluconate, 10 mM KCl, 10 mM HEPES, 0.2 mM EGTA, 4 mM ATP, 0.3 mM GTP and 10 mM phosphocreatine (pH 7.4, osmolarity: 300 mOsm). Signals were amplified using an Axon Instruments Multiclamp 200B and digitized using an Axon Instruments Digidata 1440A (Molecular Devices).

Recordings were initiated 10 minutes after membrane rupture. EPSCs were recorded by voltage-clamping the membrane potential at −70 mV (the standard reversal potential of IPSCs) and inhibiting $GABA_A$ receptor mediated currents with 20 μM bicuculline (Sigma-Aldrich). IPSC were recorded by voltage-clamping the membrane potential at +10 mV and inhibiting glutamatergic transmission with 10 μM 6-cyano-7nitroquinoxaline-2,3-dione (CNQX; TOCRIS) and 50 μM DL-2-amino-5-phosphonovaleric acid (AP-5; TOCRIS).

Miniature postsynaptic currents were recorded by the same method described above, with the addition of 1 μM tetrodotoxin (TTX; Affix scientific) to inhibit action potentials. All inhibitors were bath applied to slices at a perfusion rate of ~1 ml/min.

Recordings were analyzed offline using Clampfit 10.7 software (Molecular Devices; Sunnyvale, CA, USA). sEPSCs, mEPSCs, sIPSCs and mIPSCs were analyzed for amplitude and frequency. A separate template was created for each recording by averaging typical currents with varying detection thresholds. Data were extracted using template-based detection, and subsequently verified manually for precision.

Behavioral tests

Mice were housed on a 7:00am-7:00pm light cycle in TCP. Subject mice were handled for 1 minute on 3 consecutive days prior to first behavioral test and were allowed to acclimate to a behavioral test room for at least 30 minutes prior to tests. The age of mice was between 8 to 20 weeks old. For all tests a minimum of 8 females and 8 males were assessed per genotype.

Open field test

Mice were placed in an open field chamber (40 cm X 40 cm x 40 cm) made of plexiglass for 10 minutes. The open field chamber was in a sound attenuation box with dimmed light (75 lux). In order to test locomotor activity, mice were tracked using Activity Monitor software (Med Associates Inc.). The travel distance and time spent in center zone were analyzed.

Three-chamber social interaction test

A 60 cm x 40 cm three-chamber apparatus was located under dim light (5 lux). First, for habituation, mice explored all three chambers for 5 minutes, and then for the sociability test, once an object (an orange lid) in an empty cup had been placed in one of the side chambers and an age-, sex- and genetic background matched unfamiliar C57BL/6J mouse in the other side chamber, mice explored the chambers for 10 minutes. Finally, for the social novelty test, a novel mouse replaced the object and mice re-explored the chambers for 10 minutes. To exclude special preference, the chambers containing the object and the mouse were occasionally switched. Mice were video-tracked using the Ethovision XT software (Noldus). The time of direct interaction was measured as the amount of time the nose of the subject mouse was located within 3cm around the cup containing the stranger mouse, the familiar mouse or the object.

Reciprocal interaction

Mice were allowed to acclimate to a behavioral test room at least 30 minutes prior to tests. Two male stranger mice of the same genotype were placed together at the same time in a clean cage and allowed to interact for 5 minutes. The interactions were video recorded and then scored for the time of sniffing and touching manually in a blind condition. Statistical differences were assessed using unpaired t test.

Elevated zero maze test

Mice were placed in the middle of an open arm in the elevated zero maze (23 cm inner radius and 7 cm platform width) and their movements were video-tracked with Ethovision XT software (Noldus) for 5 minutes under dim lighting (5 lux). Time spent in open arms, the total distance traveled and the number of transitions between open and closed arms were analyzed.

Fear conditioning

During the first day mice were trained by a 2 minute period of acclimatizing to a new chamber, followed by one pairing of a tone (2800 Hz, 85 dB, 30 s) with a co-terminating foot-shock (0.75 mA for 2 s). The mice remained in the chamber for an additional 1 minute interval after the end of the last pairing, after which they were returned to their home cages. Contextual fear conditioning was assayed 24 hours after training by placing the animals in the conditioning context (same chamber where the training occurred) for a 5 minute period, during which the incidence of freezing (immobile except for respiration) was monitored using Video Freeze software (Med Associates Inc.). Auditory fear conditioning tests were performed 48 hours after training. The mice were placed into a new chamber (a triangle insert and a smooth-surfaced plastic sheet with 0.5% Acetic acid as an odor). After a 2 minute acclimation period to the new chamber (context), mice were exposed to the trained tone for 3 minutes. The fear conditioning was performed on male mice and the freezing behavior was monitored using Video Freeze software (Med Associates Inc.). Statistical analysis was based on two-way ANOVA and between-group comparisons by Tukey's post hoc test.

Marble burying test

The test apparatus for marble burying was a cage (18 cm x 36 cm x 13 cm) with 20 glass marbles (4 rows x 5 columns) on 5 cm-depth bedding surface. Mice were allowed to explore the test box for 30 minutes in a darkened room, and the number of marbles that had 50% of their surface covered by bedding was quantified.

Startle response test

Mice were placed in a recording tube in a sound attenuation chamber of the SR-LAB System (San Diego Instruments). After first 5 startle exposures, mice were randomly presented with a total of 60 trials: pre-pulse alone, pre-pulse + startle, startle alone and no stimulus. Four pre-pulse intensities were presented: 70, 75, 80 and 85 db. Pre-pulse duration was 20 ms, and pre-pulse and startle intervals ranged from 50 to 120 ms. Startle intensity was set at 120 dB for 40 to 60 ms. Each type of trial was performed 6 times. Pre-pulse inhibition (PPI%) was calculated as follows: %PPI = 100 x (S – PPi_S)/S. S and PPi_S stand for the peak amplitude of startle and pre-pulse + startle, respectively. The global level of PPI was calculated as followed; 100 x [S - (PP1_S + PP2_S + PP3_S + PP4_S)/4]/S.

Rotarod

Mice were placed on the rotating rod of a rota-rod apparatus (Harvard Apparatus) for 5 minutes. The rod was accelerating from 4 to 40 rpm. The time spent on the rod was measured for 3 trials per day for 3 consecutive days.

Resident intruder test

The subject male mice were isolated in a home cage individually for 14 days prior to tests. The singly housed mice with their home cages were transferred to a test room under dim light (10 lux). An age-matched intruder C57BL/6J male mouse was placed into the subject's home cage for 10 minutes, during which time the aggressive behavior between the subject and the intruder mouse was video-recorded by Ethovision XT software (Noldus). The number of fights, latency to start fighting and frequency of fighting were quantified under experimenter-blinded condition.

Auditory brainstem response (ABR)

Mice were anesthetized and eye drops such as Viscotears were applied to avoid drying of the cornea. Needle electrodes were placed under the skin at the top/vertex of the head (active electrode) and overlying the left bulla (bony sheath enclosing the middle ear by the mastoid bone) (reference electrode) and right bulla (ground electrode). The animal was placed within a special acoustic chamber in a natural prone position, paws forward, facing the loudspeaker at a distance of 10 cm from the leading edge of the speaker to the mouse's interaural axis. To record the ABR, a series of sound stimuli (6, 12, 18, 24, and 30 KHz) was presented to the mouse from the loudspeaker that included tone pips between the frequencies 6 and 30kHz and over levels of 0 - 85 dB (in 5dB increments).

QUANTIFICATION AND STATISTICAL ANALYSIS

Identification of conserved tissue-specific translation factors

Splicing events were defined as tissue-regulated based on a survey of RNA-Seq data from 32 human tissues or 30 mouse tissues with at least two independent samples representing each tissue (see Table S1). To comprehensively detect and quantify all AS events involving alternative exons, we used the vast-tools multi-module analysis pipeline, as previously described (Irimia et al., 2014; Tapial et al., 2017). Briefly, reads were initially mapped to genome assemblies using Bowtie, using –m 1 –c 2 parameters with reads that mapped to the genome discarded for AS quantifications. Unique EEJ (exon-exon junction) libraries were generated to derive measurements of exon inclusion levels using the metric "Percent Spliced In" (PSI). This utilized all hypothetically possible EEJ combinations from annotated and *de novo* splice sites, including cassette, mutually exclusive and microexon events (Irimia et al., 2014; Tapial et al., 2017).

Two criteria were used to score an AS event as tissue-dependent. First, at least 20 mapped reads were required to support the event. Second, a statistically robust PSI difference of > 20% between a given tissue and all other tissue samples was required, as measured using the *diff* module of vast-tools for differential PSI quantification (https://github.com/vastgroup). An event was considered conserved if it displayed differential splicing between equivalent tissues in both human and mouse samples. Only annotated genes within the GO term class "translation" (GO:0006412) were considered as "Translation Factors." The heatmap was constructed using the R and after scaling by row (subtracting the mean (centering) and dividing by standard deviation (scaling)).

PsychENCODE data analysis

Data for the Figures 2F and S2I-G were obtained from NIMH Reporsitory & Genomic Resources, a centralized national bioreporsitory for genetic studies of psychiatric disorders. RNA-Seq data from autism spectrum disorder and control post-mortem samples were downloaded from the UCLA-ASD's PsychENCODE data storage. When fastq files were not available, bam files were converted to fastq using samtools ("samtools sort" followed by "samtools fixmate" and finally "samtools fastq" (with –t and –O tags)). Files were assessed using fastqc and adapters identified removed by Trimmomatics. Gene expression and alternative splicing quantification were performed using Whippet (https://github.com/timbitz/Whippet.jl) with default setting and an index (–suppress-low-tsl) based on Ensembl hg38. Microexons were extracted based on size. Median of controls was calculated and subtracted from each ASD sample to identify the most strongly disrupted microexons.

Computational detection of prion-like and intrinsically disordered regions in eIF4G proteins

The web-based prion prediction algorithm PLAAC (Prion-like amino acid composition) was applied to detect prion-related domains in human eIF4G1 and eIF4G3 (Lancaster et al., 2014) with amino acid distribution estimated using the setting (α 100) for weighting of background probabilities. PLAAC is also a predictor for phase separation (Vernon and Forman-Kay, 2019). To detect low complexity regions in human eIF4G1 and eIF4G3 we applied DISOPRED3 using the PSIPRED protein analysis workbench (Jones and Cozzetto, 2015). Figures 6A and S6A were generated as described in Bakthavachalu et al. (2018).

Quantitative proteomics data analysis

The Proteome Discoverer 2.1.0.81 software (Thermo Fisher Scientific) was used for analyses of RAW files. Searching was performed using The SEQUEST HT database search engine and the mouse proteome database (SwissProt TaxID = 10090, 2016-05-11) downloaded from ProteinCenter supplemented with a list of common contaminants derived from ProteinCenter (PD_Contaminants_2014_11). Both the forward and reversed databases were used for database searches in order to evaluate the false discovery rates (FDRs); 50,346 total entries were searched. Trypsin was selected as the digestion enzyme and a maximum number of two missed

cleavages were allowed. The mass tolerance of precursor ions and fragment ions were set as 10 ppm and 0.08 Da, respectively. The iTRAQ 8 plex (peptide N terminus and lysine) and carbamidomethylation (cysteine) were set as the static modifications. Acetylation (Protein N-terminus), Oxidation (methionine) and deamination (Asparagine or Glutamine) were chosen as the dynamic modifications. The Percolator tool integrated in the Proteome Discoverer 2.1 software was used to validate the database search results based on the q-value. The identifications were filtered with peptide confidence value as high to obtain FDR less than 1% on the peptides level. Protein grouping was enabled, and the strict parsimony principle was applied.

Proteins identified and quantified in all three biological replicates were delivered to Benjamini-Hochberg (BH) FDR estimations, and those that passed the 1% BH-FDR threshold and with a log2 ratio < -0.25 or > 0.25 were considered as significant changes.

Mass spectrometry data generated in this study have been deposited at the ProteomeXchange consortium through partner MassIVE (https://massive.ucsd.edu/ProteoSAFe/static/massive.jsp). The data have been assigned ID MSV000084658.

Heatmap of MS data

Only detected proteins with a 1% pass rate were considered. The normalized abundance ratios (log(DKO/WT+1)) were calculated. The heatmap was generated using R from the abundance ratio of DKO/WT for each replicate.

Functional enrichment analysis

Functional enrichment analysis was performed using the functional enrichment analysis tool g:Profiler (https://biit.cs.ut.ee/gprofiler) (Reimand et al., 2016). Structured controlled vocabularies from Gene Ontology, as well as information from the curated KEGG and Reactome databases were included in the analysis. Only functional categories with more than three members and fewer than 2,000 members were included in the analysis. Significance was assessed using the hypergeometric test with multiple testing correction by the Benjamini and Hochberg method. The Cytoscape plug-in Enrichment map (http://baderlab.org/Software/EnrichmentMap) (Isserlin et al., 2014) was used to visualize and arrange functional data. In enrichment maps, node size is proportional to the number of genes associated with the GO category, and edge width is proportional to the number of genes shared between GO categories. Node clusters are arranged to contain similar functional terms.

For enrichment analysis, rat genes enriched in the neuropil were extracted from data supplied by Cajigas et al. (2012). BioMart was used to identify one-to-one rat to mouse orthologs. Synaptic-related genes were downloaded from SynaptomeDB (http://metamoodics.org/SynaptomeDB (04/2018) (Pirooznia et al., 2012). Statistical enrichment was assessed using Fisher's exact test and corrected for multiple hypothesis testing (when applicable).

BioID mass spectrometry data analysis

Mass spectrometry data was stored, searched and analyzed using the ProHits laboratory information management system (LIMS) platform (Liu et al., 2016). Briefly, the WIFF data files were converted to MGF format using WIFF2MGF and subsequently converted to an mzML format using ProteoWizard (3.0.4468) and the AB SCIEX MS Data Converter (V1.3 beta). The mzML files were next searched using Mascot (v2.3.02) and Comet (2014.02 rev.2) against a protein database of 58,206 total proteins consisting of the NCBI mouse RefSeq database (v53, Sep 9th, 2015, forward and reverse sequences) supplemented with ''common contaminants'' from the Max Planck Institute (https://141.61.102.106:8081/share.cgi?ssid=0f2gfuB) and the Global Proteome Machine (https://www.thegpm.org/crap/index.html) as well as sequences from common fusion proteins and epitope tags. Search parameters were set for tryptic cleavages, allowing up to 2 missed cleavage sites per peptide, MS1 mass tolerance of 40 ppm with charges of 2+ to 4+ and an MS2 mass tolerance of ± 0.15 amu. Asparagine/glutamine deamidation and methionine oxidation were selected as variable modifications. The results from each search engine were jointly analyzed through the Trans-Proteomic Pipeline (TPP) (Deutsch et al., 2010) via the iProphet pipeline (Shteynberg et al., 2011). A minimum iProphet probability of 0.95 was required for protein identification with 2 unique peptides required for protein interaction scoring.

Significance Analysis of INTeractome (SAINTexpress version 3.6.1) (Teo et al., 2014) was used as a statistical tool to calculate the probability of each potential proximity interaction compared to control samples (BirA*-Flag-GFP, and BirA*-Flag-empty, each run in two biological replicates). For each biological replicate, counts for each protein in a given bait sample were analyzed independently against control samples before averaging of the score values and assessment of the Bayesian False Discovery Rates (BFDR) (Teo et al., 2014). High-confidence interactions are defined as those with FDR $\leq$ 5%.

Mass spectrometry data generated in this study, including the complete SAINTexpress results, have been deposited at the ProteomeXchange consortium through partner MassIVE (https://massive.ucsd.edu/ProteoSAFe/static/massive.jsp). The data have been assigned IDs MSV000083349 and PXD012421.

BioID data visualization

Spectral counts for both eIF4G1 splice variants BioID samples were calculated by averaging counts for both biological replicates and subtracting the average counts across all controls. To be included in the analysis, a protein was required to be identified with a minimum of 10 average counts and meeting the 5% BFDR threshold in at least one of the isoforms. For the bar plots, the proteins were sorted according to the average spectral count ratios across the eIF4G1+MIC and eIF4G1ΔMIC BioID experiments. Each protein was annotated according to whether it is an mRNP cytoplasmic granule protein based on recently published datasets (Youn et al., 2018) (Figure 6B), and significant differences in the spectral count ratios of proteins detected as associated with cytoplasmic granule components were compared using the Mann-Whitney U-test. BioID spectral count data for both eIF4G1 splicing variants was visualized

as a 'dotplot' (Figure 6B) representation using the ''dotplot'' generator tools available through ProHits-viz (Knight et al., 2017). Color intensity represents the averaged count data across replicates, the circle edge shows the respective BFDR thresholds as calculated by SAINTexpress, and the size of the circle is proportional to the relative counts between splice variants (after averaging counts between replicates) with the larger size representing the maximum value.

For all positions in a protein a score for intrinsic disorder was computed using IUPred (http://iupred.enzim.hu). Amino acid residues with a score larger than 0.5 were considered disordered. Prion-like regions were identified using PLACC (prion-like amino acid composition) with amino acid distribution estimated using the setting (α 50) for weighting of background probabilities (Lancaster et al., 2014). Proteins preferentially associated with the eIF4G1+MIC isoform were defined as those that have at least a 1.25-fold difference in the ratio of spectral counts between the +MIC/ΔMIC splice variants. Proteins preferentially associated with eIF4G1ΔMIC were defined as those that have a ratio of spectral counts between the +MIC/ΔMIC splice variants of less than one.

iCLIP-Seq analysis

Analysis of iCLIP-Seq data was performed as previously described (Han et al., 2017). 51-nt raw reads that consisted of 3 random positions, a 4-nt multiplexing barcode, and another 2 random positions, followed by the cDNA sequence, were initially de-duplicated based on the first 45 nt. Reads were de-multiplexed and the random positions, barcodes, and any 3′-bases matching Illumina adaptors were removed. Finally, reads shorter than 25 nt were filtered out and remaining reads trimmed to 35 nt. These steps were carried out using Trimmomatic (Bolger et al., 2014). Remaining reads were mapped to the mouse genome/transcriptome (Ensembl annotation of NCBIm37) using tophat (Trapnell et al., 2009) with default settings. To prevent false assignments of reads from repetitive regions, any reads with a mapping quality < 3 were removed from further analysis. Plots showing average crosslinking signal of events aligned to exon boundaries were generated as described after first reducing reads to their first position, which is adjacent to the crosslink position. A 21-bp running window average was used for plotting, and average signals across replicates are shown.

RNA sequencing and ribosome profiling data analysis

All fastq files were quality checked using FastQC. Trimmomatics was used to remove adaptors and low-quality reads. Reads were first aligned with Bowtie to human or mouse rRNA sequences, and matches were discarded (–v 3). Processed RNA-seq reads were aligned to the mouse genome (mm10) using whole genome alignment by STAR with 2-pass setting enabled and output in bam format. In addition, mRNA expression levels were calculated using kallisto (Bray et al., 2016) with transcripts downloaded from Ensembl mm10 and filtered for support level > 3. Kallisto was run on default settings with k = 25 and pseudobam output.

For differential mRNA expression analysis, read counts for each gene were calculated using vast-tools (Irimia et al., 2014; Tapial et al., 2017) and analyzed with DESeq (Anders and Huber, 2010) (unless mentioned otherwise: adjusted p value < 0.05 and > 0.5 absolute fold change). Genes showing differential regulation during KCl-mediated activity dependence were identified by reanalyzing raw sequencing data from Quesnel-Vallières et al. (2016) using the vast-tools pipeline. Statistical enrichment of genes with transcript level changes in Eif4g DKO neurons with those regulated by KCl treatment was assessed using Fisher's exact test.

To detect changes in translational efficiency per gene, RiboDiff (Zhong et al., 2017) was employed with default settings using combined read counts from Kallisto. The R package RiboSeqR (https://bioconductor.org/packages/release/bioc/html/riboSeqR.html) was used to identify reading frames and confirm the periodicity of the ribosome profiling data. Default settings were used in RiboSeqR with only canonical start and stop codons considered. To identify pausing sites, the algorithm PausePred (Kumari et al., 2018) was used with default settings. Only protein-coding genes within annotated transcripts were considered. Only genes with a 50% increase/decrease in number of pausing events were included in downstream analysis.

Overlap of paused genes in Eif4g DKO and *Fmr1* KO neurons

Ribosome profiling data from Eif4g DKO neurons (this study) and *Fmr1* KO adult hippocampal neural stem cells (Liu et al., 2018; GSE112502 samples) were analyzed using the PausePred (Kumari et al., 2018) algorithm (after trimming/rRNA removal and STAR alignment) with the same cutoffs as described above. Sites identified as paused in both datasets were compared to a background set of genes, corresponding to those genes detected in the ribosome profiling data (TPM > 1) and analyzed by PausePred.

High confidence FMRP targets were determined as those with at least 10 FMRP HITS-CLIP peaks in brain tissue (Maurin et al., 2018). Statistical enrichment was assessed using Fisher's exact test and corrected for multiple hypothesis testing.

Motif enrichment in Eif4g DKO paused genes

High quality pause sites (score > 50) identified by PausePred (Kumari et al., 2018) were extracted and sequences 50 nucleotides upstream and downstream used in the analysis. CentriMO (Bailey and Machanick, 2012) was used to search for motif enrichment (—local). No hits (adj-p < 1e-3) were found when upstream sequences were analyzed. However, strong motif enrichments (adj-p < 1e-3) were identified when analyzing sequences downstream of the pause sites, both when using the default background (data not shown) and when using sequences upstream of the pause site as background (Figure 6F). In Figure 6F only recognition motifs corresponding to RNA binding proteins involved in translation regulation (GO:0006417) were analyzed (Ray et al., 2013).

Quantification of stalled ribosomes from micrographs

Images of 53 WT and 53 Eif4g microexon-DKO neurons from two independent preparations were captured using a Zeiss fluorescent microscope and Zen software. Images were analyzed in batches with "find maxima" function of ImageJ to detect and mark stalled ribosome granules. Reported counts were then manually corrected to remove counts from neighboring cells. Data were analyzed for significant differences using Mann-Whitney U test.

Foci Quantification

The transfected SH-SY5Y cells were binned into two groups: those showing diffuse cytoplasmic distribution of mCherry signal ("Dispersed") and those with concentrated puncta-like mCherry signal ("Foci"). For each construct, over 400 transfected cells were analyzed (total cells: eIF4G1+MIC, 420 cells; eIF4G1ΔMIC 581 cells) and experiments were performed in triplicate. Data were analyzed using a two-way analysis of variance (ANOVA) and Tukey's post hoc test.

Statistics for behavioral testing

One-way ANOVA, Two-way ANOVA, or two-tailed t test were performed for all the behavior analysis.
Tukey test was performed as a post hoc test.

Related to 3-chamber sociability test (Figure S4J)

Two-way ANOVA chamber main effect, $F(2, 120) = 228.3$, $p < 0.0001$.
Tukey's post hoc test:
Male WT: Object versus Male WT: Mouse p = 0.0019,
Male *Eif4g1*$^{\Delta MIC/\Delta MIC}$: Object versus Male *Eif4g1*$^{\Delta MIC/\Delta MIC}$: Mouse p = 0.0040,
Female WT: Object versus Female WT: Mouse p = 0.0203,
Female *Eif4g1*$^{\Delta MIC/\Delta MIC}$: Object versus Female *Eif4g1*$^{\Delta MIC/\Delta MIC}$: Mouse p = 0.0001.

Related to 3-chamber social novelty test (Figures 4B and S4K)

Two-way ANOVA: chamber main effect $F(2, 66) = 79.54$, *** $P < 0.0001$.
Figure 4B: Tukey's post hoc test:
Male WT: Familiar mouse versus Male WT: Stranger mouse p = 0.0196;
Male *Eif4g1*$^{\Delta MIC/\Delta MIC}$: Familiar mouse versus Male *Eif4g1*$^{\Delta MIC/\Delta MIC}$: Stranger mouse p = 0.9133,
Figure S4K: Tukey's post hoc test:
WT:Familiar mouse versus WT: Stranger mouse p = 0.0196,
Eif4g1$^{\Delta MIC/+}$: Familiar mouse versus *Eif4g1*$^{\Delta MIC/+}$: Stranger mouse p = 0.2095,
Eif4g1$^{\Delta MIC/\Delta MIC}$: Familiar mouse versus *Eif4g1*$^{\Delta MIC/\Delta MIC}$: Stranger mouse p = 0.9133.

Related to reciprocal interaction test (Figure 4C)

1 min: Male *Eif4g1*$^{\Delta MIC/\Delta MIC}$ versus Male *Eif4g1*$^{\Delta MIC/\Delta MIC}$ nose-to-nose sniffing; ** p = 0.0011,
1 min: Male WT versus Male WT touching frequency; p = 0.5570,
5 min: Male *Eif4g1*$^{\Delta MIC/\Delta MIC}$ versus Male *Eif4g1*$^{\Delta MIC/\Delta MIC}$ nose-to-nose sniffing; * p = 0.0384,
5 min: Male WT versus Male WT touching frequency; p = 0.17.

Related to fear conditioning test (Figure 4E)

Contextual fear conditioning: 2-way ANOVA genotype main effect, $F(2, 126) = 132.1$;
Tukey's post hoc test:
1 min: Male WT versus 1 min: Male *Eif4g1*$^{\Delta MIC/\Delta MIC}$ ** p = 0.0036;
1 min: Male WT versus 1 min: Male *Eif4g1*$^{\Delta MIC/+}$ ** p = 0.0057;
2 min: Male WT versus 2 min: Male *Eif4g1*$^{\Delta MIC/\Delta MIC}$ ** p = 0.0035.
Cued fear conditioning: Two-way ANOVA time main effect, $F(4, 165) = 13.74$, $p < 0.0001$; genotype main effect $F(2, 165) = 1.013$, p = 0.3653.

DATA AND CODE AVAILABILITY

The accession numbers for Illumina iCLIP-Seq, RNA-Seq and Ribo-Seq data reported in this study are Gene Expression Omnibus (GEO): GSE141594, GSE141599 and GSE141599, respectively. Mass spectrometry data generated in this study have been deposited at the ProteomeXchange Consortium through partner MassIVE and have been assigned IDs MSV000083349 / ProteomeXchange: PXD012421 (BioID) and MSV000084658 (iTRAQ). Scripts are available upon request.